Article

Current Biology

Intracytoplasmic-membrane development in alphaproteobacteria involves the homolog of the mitochondrial crista-developing protein Mic60

Highlights

- Mic60's predicted structure is conserved in alphaproteobacteria
- Mic60 disruption decreases photoheterotrophic growth rate
- Mic60 disruption and overexpression affects ICM development
- Mic60 physically interacts with BamA in alphaproteobacteria

Authors

Sergio A. Muñoz-Gómez, Lawrence Rudy Cadena, Alastair T. Gardiner, ..., Claudio H. Slamovits, Julius Lukeš, Hassan Hashimi

Correspondence

samunozg@purdue.edu (S.A.M.-G.), hassan@paru.cas.cz (H.H.)

In brief

The Mic60 protein anchors and compartmentalizes mitochondrial cristae in eukaryotes. Muñoz-Gómez et al. show that the alphaproteobacterial Mic60 homolog is involved in the development of intracytoplasmic membranes (ICMs) and that the Mic60-BamA interaction has been conserved. These findings lend support to the notion that cristae evolved from ICMs.

Muñoz-Gómez et al., 2023, Current Biology *33*, 1–13
March 27, 2023
https://doi.org/10.1016/j.cub.2023.02.059

CellPress

Please cite this article in press as: Muñoz-Gómez et al., Intracytoplasmic-membrane development in alphaproteobacteria involves the homolog of the mitochondrial crista-developing protein Mic60, Current Biology (2023), https://doi.org/10.1016/j.cub.2023.02.059

Current Biology

CellPress

Article

Intracytoplasmic-membrane development in alphaproteobacteria involves the homolog of the mitochondrial crista-developing protein Mic60

Sergio A. Muñoz-Gómez,[1,9,10,11,*] Lawrence Rudy Cadena,[2,3,9] Alastair T. Gardiner,[4] Michelle M. Leger,[5] Shaghayegh Sheikh,[2,3] Louise B. Connell,[6] Tomáš Bílý,[2,3] Karel Kopejtka,[4] J. Thomas Beatty,[7] Michal Koblížek,[4] Andrew J. Roger,[8] Claudio H. Slamovits,[8] Julius Lukeš,[2,3] and Hassan Hashimi[2,3,*]

[1]Department of Biological Sciences, Purdue University, West Lafayette, IN 47907, USA
[2]Institute of Parasitology, Biology Center, Czech Academy of Sciences, 37005 České Budějovice (Budweis), Czech Republic
[3]Faculty of Science, University of South Bohemia, 37005 České Budějovice (Budweis), Czech Republic
[4]Center Algatech, Institute of Microbiology, Czech Academy of Sciences, 37901 Třeboň, Czech Republic
[5]Institute of Evolutionary Biology (CSIC-Universitat Pompeu Fabra), Barcelona, 08003 Catalonia, Spain
[6]Department of Chemistry and Biomolecular Sciences, University of Ottawa, Ottawa, ON K1N 6N5, Canada
[7]Department of Microbiology and Immunology, University of British Columbia, Vancouver, BC V6T 1Z3, Canada
[8]Centre for Comparative Genomics and Evolutionary Bioinformatics, Department of Biochemistry and Molecular Biology, Dalhousie University, Halifax, NS B3H 4R2, Canada
[9]These authors contributed equally
[10]Twitter: @sergiophyceae
[11]Lead contact
*Correspondence: samunozg@purdue.edu (S.A.M.-G.), hassan@paru.cas.cz (H.H.)
https://doi.org/10.1016/j.cub.2023.02.059

SUMMARY

Mitochondrial cristae expand the surface area of respiratory membranes and ultimately allow for the evolutionary scaling of respiration with cell volume across eukaryotes. The discovery of Mic60 homologs among alphaproteobacteria, the closest extant relatives of mitochondria, suggested that cristae might have evolved from bacterial intracytoplasmic membranes (ICMs). Here, we investigated the predicted structure and function of alphaproteobacterial Mic60, and a protein encoded by an adjacent gene Orf52, in two distantly related purple alphaproteobacteria, *Rhodobacter sphaeroides* and *Rhodopseudomonas palustris*. In addition, we assessed the potential physical interactors of Mic60 and Orf52 in *R. sphaeroides*. We show that the three α helices of mitochondrial Mic60's mitofilin domain, as well as its adjacent membrane-binding amphipathic helix, are present in alphaproteobacterial Mic60. The disruption of Mic60 and Orf52 caused photoheterotrophic growth defects, which are most severe under low light conditions, and both their disruption and overexpression led to enlarged ICMs in both studied alphaproteobacteria. We also found that alphaproteobacterial Mic60 physically interacts with BamA, the homolog of Sam50, one of the main physical interactors of eukaryotic Mic60. This interaction, responsible for making contact sites at mitochondrial envelopes, has been conserved in modern alphaproteobacteria despite more than a billion years of evolutionary divergence. Our results suggest a role for Mic60 in photosynthetic ICM development and contact site formation at alphaproteobacterial envelopes. Overall, we provide support for the hypothesis that mitochondrial cristae evolved from alphaproteobacterial ICMs and have therefore improved our understanding of the nature of the mitochondrial ancestor.

INTRODUCTION

Mitochondria are organelles inferred to have been present in the last common ancestor of all eukaryotes.[1] Unlike most other organelles, the mitochondrion evolved from an endosymbiont most closely related to extant alphaproteobacteria.[2–4] In aerobic eukaryotes, mitochondria produce most intracellular ATP through aerobic respiration. Because aerobic respiration occurs at expanded internalized membranes, mitochondria allow for the proportional increase of respiration with cell volume across eukaryotes.[5] Mitochondria are thus among the innovations that likely allowed eukaryotes to achieve larger cell volumes without compromising relatively fast growth rates. This ultimately opened new evolutionary trajectories. Elucidating the origin of mitochondria and their respiratory membranes may shed light on the origin of eukaryotes.

The specialization of mitochondria as respiratory organelles is most clearly reflected in their internal structure. The mitochondrial inner membrane invaginates into specialized subcompartments called cristae, the structural hallmarks of the organelle.[6–8] The mitochondrial contact site and cristae organizing system (MICOS) complex and F_1F_O-ATP synthase oligomers are two

Please cite this article in press as: Muñoz-Gómez et al., Intracytoplasmic-membrane development in alphaproteobacteria involves the homolog of the mitochondrial crista-developing protein Mic60, Current Biology (2023), https://doi.org/10.1016/j.cub.2023.02.059

of the most evolutionarily conserved factors responsible for crista development and shape.[9,10] Whereas ATP synthase oligomers bend crista membranes at their rims to produce diverse shapes,[11,12] the MICOS complex creates both crista junctions and contact sites that compartmentalize, stably anchor, and maintain cristae at the mitochondrial envelope.[13] These MICOS functions appear to be conserved across phylogenetically disparate eukaryotes, such as in animals, fungi, land plants, and parasitic protists.[14–17]

Studies on MICOS evolution revealed that it is ancestrally present in all eukaryotes and predates the origin of mitochondria.[18,19] The central and scaffolding subunit of the MICOS complex, Mic60, traces back to the *Alphaproteobacteria*, the group from which mitochondria descended. Indeed, Mic60 serves as a phylogenetic marker that is restricted to the *Alphaproteobacteria* and the mitochondrial lineage.[2] While only Mic60's C-terminal signature mitofilin domain is sufficiently conserved at the sequence level, the overall predicted secondary structure of Mic60 is also conserved in mitochondrial and alphaproteobacterial homologs.[18] In addition to having Mic60 homologs, many alphaproteobacteria also develop either lamellar or vesicular intracytoplasmic membranes (ICMs) that house diverse electron transport chains involved in methanotrophy (methane oxidation), nitrification (nitrite oxidation), and (aerobic or anaerobic) anoxygenic photosynthesis.[20–24] This raises the possibility that Mic60 is involved in the development and/or stability of ICMs in alphaproteobacteria and that mitochondrial cristae evolved from ancestral alphaproteobacterial ICMs.[25] Support for the functional conservation of alphaproteobacterial Mic60 comes from its capacity to bind and bend membranes *in vitro* and heterologously in the gammaproteobacterium *Escherichia coli*.[26] However, the precise role of Mic60 has not yet been directly studied in alphaproteobacteria. Thus, the evolutionary relationship between cristae and ICMs remains unknown.

Even though early ideas linked cristae to ICMs based simply on morphological resemblance, the iconography of the field typically depicts cristae as post-endosymbiotic adaptations of mitochondria.[25] To better understand the function of Mic60 in alphaproteobacteria and the origin of mitochondrial cristae, we investigated the role of *mic60*, and its adjacent gene *orf52*, in two distantly related purple alphaproteobacteria: the vesicular ICM-developing *Rhodobacter* (*Cereibacter*) *sphaeroides* (*Rhodobacterales*) and lamellar ICM-developing *Rhodopseudomonas palustris* (*Rhizobiales*). We first explored the genomic context, large-scale phylogenetic distribution, and structural conservation of alphaproteobacterial Mic60 homologs. We then experimentally investigated the effects of the disruption and overexpression of Mic60 and Orf52 in photoheterotrophic growth and ICM development. Finally, we assessed the higher-order assembly and physical interactors of alphaproteobacterial Mic60 and Orf52.

RESULTS

The genomic clustering of *mic60* and its adjacent *orf52* gene is conserved across the *Alphaproteobacteria*

A survey of *mic60*'s genomic context in several alphaproteobacterial species revealed that *mic60* is genetically linked to genes involved in the heme biosynthesis pathway.[19] In most genomes, *mic60* is downstream of *hemC* (hydroxymethylbilane synthase [HMBS]) and *hemD* (uroporphyrinogen-III synthase [UROS]) and upstream of a conserved syntenic protein-coding gene. All four genes have the same orientation and are usually tightly clustered with little intergenic space, suggesting that they are functionally related and/or co-transcribed as part of the same operon. This is consistent with the regulatory requirements of Mic60 toward its hypothesized function in ICM development, which requires heme biosynthesis for cytochrome assembly.[25] Indeed, HemD is occasionally fused to Mic60 in members of the *Rhodospirilales*, *Kiloniellales*, and *Rhizobiales* (Figure 1A).[19] In the yeast *Sacchromyces cerevisiae*, MICOS was reported to interact with ferrochelatase (HemH in alphaproteobacteria), which catalyzes the final step in heme biosynthesis.[27]

Although *hemC* and *hemD* are genuine heme biosynthesis enzymes, the gene downstream of *mic60* does not likely encode a heme biosynthetic enzyme. This protein is usually misannotated as HemY because it contains a conserved hemY_N domain (PF07219) at its N terminus. Confusingly, this domain is unrelated to genuine *hemY* (protoporphyrinogen IX oxidase), which is rather uncommon among alphaproteobacteria.[28] Here, the protein encoded by the gene downstream of *mic60* will be referred to as Orf52, based on its predicted size of 52 kDa in *R. sphaeroides*. Like alphaproteobacterial Mic60, Orf52 is an integral membrane protein but possesses two transmembrane segments instead of one at its N terminus and seems to expose its bulk to the periplasmic space. Moreover, Orf52 contains several tetratricopeptide repeat motifs, which are usually involved in protein-protein interactions and found in subunits of multi-protein complexes. In *R. sphaeroides*, the *mic60-orf52* gene pair is co-transcribed as indicated by a transcription start site (TSS) in the intergenic region between *hemD* and *mic60*[29] (Figure 1A). In the magnetosome gene island (MAI) of *Magnetospirillum gryphiswaldense*, *mic60* and *orf52* are also co-transcribed separately from adjacent genes.[30] The conserved motif order and composition of Mic60 and Orf52, as well as their transcriptional coupling, indicate that these proteins have structural roles and may physically interact at alphaproteobacterial envelopes.

Mic60 and Orf52 have broad phylogenetic distributions that overlap with the distribution of ICMs in the *Alphaproteobacteria*

Prokaryotic Mic60 homologs have been previously shown to be restricted to alphaproteobacterial species, thus serving as a synapomorphy for the clade that comprises both mitochondria and the *Alphaproteobacteria*.[2,18,19] Moreover, phylogenetically diverse alphaproteobacteria are known to develop extensive bioenergetic ICMs.[20–25] However, it is unclear to what extent the presence of Mic60 correlates with the occurrence of ICMs. To better understand the relationship between Mic60 and ICMs, we investigated their large-scale phylogenetic distributions in the *Alphaproteobacteria*. Therefore, we searched the GTDB R207 database that currently comprises >7,684 alphaproteobacterial genomes with profile hidden Markov models (pHMMs) for Mic60, Orf52, and markers for ICM-associated physiologies (Figure 1B).

These analyses show that Mic60 and Orf52 have a broad and dense phylogenetic distribution that encompasses the much more sporadic distribution of reported ICMs in the

Please cite this article in press as: Muñoz-Gómez et al., Intracytoplasmic-membrane development in alphaproteobacteria involves the homolog of the mitochondrial crista-developing protein Mic60, Current Biology (2023), https://doi.org/10.1016/j.cub.2023.02.059

CellPress

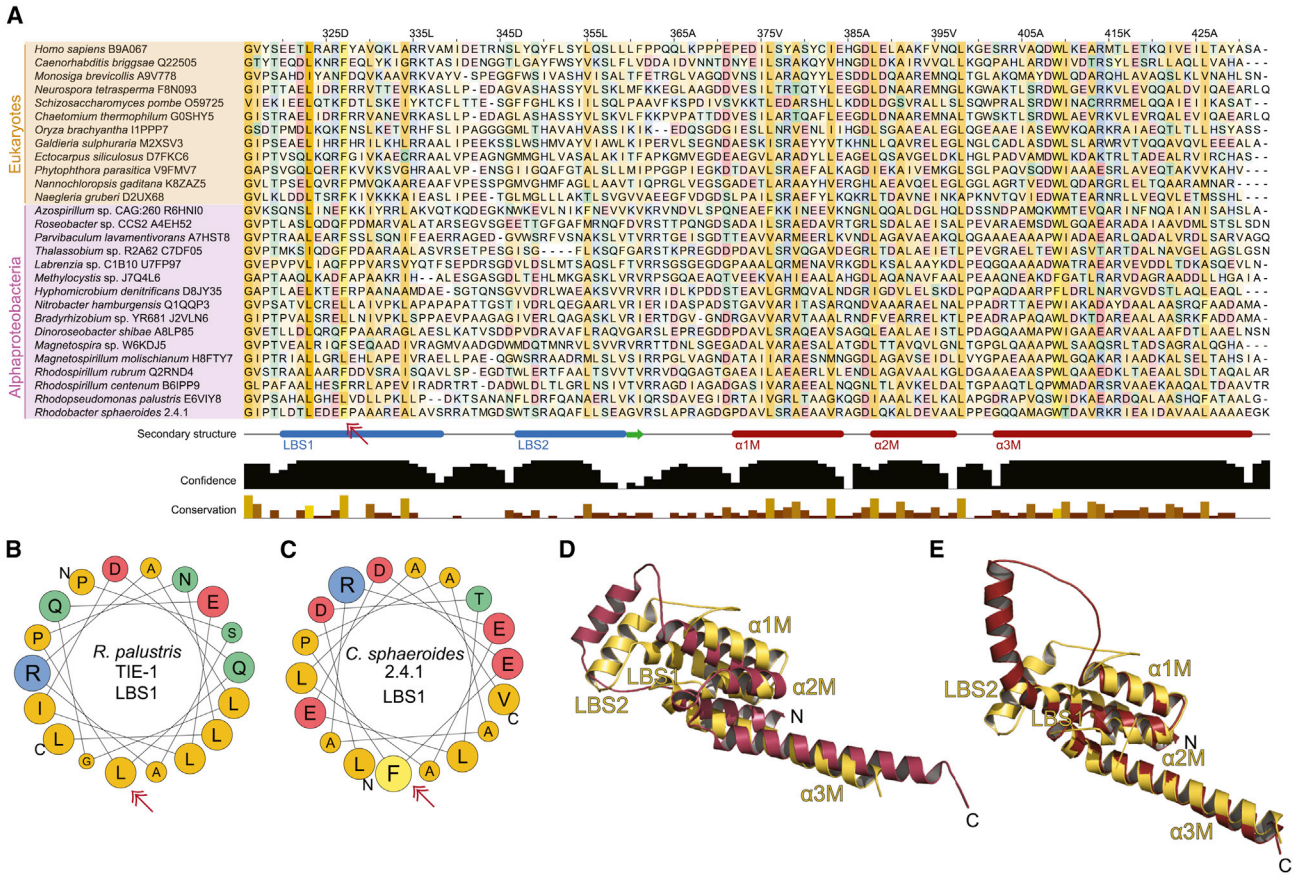

Figure 1. Genomic context of *mic60* and phylogenetic distribution of Mic60, Orf52, and ICMs across the *Alphaproteobacteria*

(A) The genomic context for *mic60* in representative ICM-developing alphaproteobacteria and their relatives. Black circles to right of species identifiers denote alphaproteobacteria that develop extensive ICMs. The bent arrow denotes the TSS in *R. sphaeroides*.

(B) A comprehensive phylogenetic tree of the *Alphaproteobacteria* that displays the distributions of Mic60, Orf52, markers for ICM-associated physiologies, and reported ICMs across a maximally diverse set of taxa, as detailed in STAR Methods.

Alphaproteobacteria (Figure 1B). Methanotrophy and nitrite oxidation are restricted to very few genera (e.g., *Methylocella*, *Methylosinus*, *Methylocystis*, and *Nitrobacter*), whereas photoautotrophy is phylogenetically widespread (Figure 1B). The presence of these ICM-associated physiologies largely overlaps with those species reported to develop extensive ICMs (Figure 1B). The prediction of a photoautotrophic physiology in several species not yet examined ultrastructurally suggests that these too may develop ICMs. On the other hand, aerobic anoxygenic photoheterotrophs are phylogenetically much more broadly distributed in the *Alphaproteobacteria*[31] (Figure 1B), although they do not often have extensive ICMs; some aerobic phototrophs can develop less conspicuous ICMs under some environmental conditions.[32] Altogether, these phylogenetic patterns suggest that Mic60 and Orf52 are ancestrally present in the *Alphaproteobacteria* and are required by extant species that either have or lack the capacity to develop ICMs.

The predicted secondary and tertiary structure of alphaproteobacterial Mic60 is conserved

Previous studies demonstrated that the overall predicted secondary structure of Mic60 is conserved both in eukaryotes and alphaproteobacteria.[18,19] In the former, Mic60 consists of an N-terminal mitochondrion-targeting pre-sequence, followed by a transmembrane segment, central region with coiled coils, and C-terminal signature mitofilin domain. The same secondary structure is found in alphaproteobacterial Mic60, minus the N-terminal pre-sequence. Recently, mitochondrial Mic60 has been shown to deform membranes and thus likely to introduce curvature at crista junctions.[26,33] This membrane-deforming capability depends on a lipid-binding site (LBS) that is found in between the central coiled coils and C-terminal mitofilin domain. This LBS comprises two α helices, LBS1 and LBS2. Amphipathic LBS1 presumably inserts itself into the mitochondrial inner membrane. This motif is extremely important for Mic60's function, as LBS1 removal or mutation leads to the loss of membrane binding and deformation and also to phenotypes similar to those from *MIC60* gene deletion in *S. cerevisiae*.[33]

To investigate whether the membrane-bending α helices of eukaryotic Mic60 are present in its alphaproteobacterial homologs, we first performed pHMM-sequence searches against the UniProtKB database. We also predicted the secondary structures of both eukaryotic and alphaproteobacterial Mic60 homologs with JPred4.[34] A detailed inspection of both

Please cite this article in press as: Muñoz-Gómez et al., Intracytoplasmic-membrane development in alphaproteobacteria involves the homolog of the mitochondrial crista-developing protein Mic60, Current Biology (2023), https://doi.org/10.1016/j.cub.2023.02.059

alignments and predicted secondary structures revealed that alphaproteobacterial Mic60 also has the two α helices that comprise the LBS (Figure 2A). Helical wheel projections further show that LBS1 is amphipathic in both *R. sphaeroides* and *R. palustris* (Figures 2B and 2C). In addition, the functionally critical amino acid position Phe573 in the yeast *Chaetomium thermophilum*[33] is largely conserved among alphaproteobacteria (e.g., Phe327 in *R. sphaeroides*; Figure 2A).

Next, we predicted the tertiary structure of the Mic60 homologs of the yeast *Lachancea thermotolerans*, whose crystal structure was partially solved,[36] and *R. sphaeroides* and *R. palustris*, using AlphaFold2 (Figure S1). The predicted structures confirm the presence of the two α helices (LBS) in the linker region between the central coiled coils and the C-terminal mitofilin domain (Figure S1). Furthermore, the predicted structures show that the three conserved α helices that comprise the mitofilin domain of eukaryotic Mic60 (α1-3M), plus the last two small α helices of the central coiled-coil region (α2-3C), are also present in alphaproteobacterial Mic60. Structural alignments reveal that the C-terminal region of alphaproteobacterial Mic60 (i.e., LBS + mitofilin) largely overlaps with that of its eukaryotic homolog (Figures 1D and 1E). The major structural differences between eukaryotic and alphaproteobacterial Mic60 homologs are that the former is, on average, a longer protein with a larger central coiled-coil segment and that it has a transmembrane domain (TMD) much closer to the N terminus (Figure S1). The agreement between the predicted AlphaFold2 structure with high-confidence pLDDT scores and the partially solved structure at amino acids 207–382[36] suggests that eukaryotic Mic60 indeed folds into a long α1C helix (Figure S1B). On the other hand, alphaproteobacterial Mic60 may similarly have a long α1C helix, but the lower pLDDT scores in this region make this prediction uncertain (Figure S1D). In summary, these observations indicate that alphaproteobacteria Mic60 (1) has a largely conserved secondary and tertiary structure relative to eukaryotic Mic60 and (2) contains a conserved amphipathic LBS1 helix that likely aids in membrane binding and bending, as demonstrated *in vitro* for its eukaryotic ortholog.[26,33]

Knockout of *mic60* and *orf52* significantly affects photoheterotrophic growth of *R. sphaeroides* and *R. palustris*

Purple alphaproteobacteria develop extensive ICMs in the presence of light and the absence of oxygen.[20,21,37] These ICMs house the photosynthetic apparatus and electron transport chain, which is generally composed of light-harvesting complexes 1 and 2 (LH1 and LH2), a type II reaction center (RC), a cytochrome bc_1, a periplasmic cytochrome c_2, and an ATP synthase.[38] By means of cytochrome bc_1, which is also shared with the respiratory chain, the photosynthetic chain creates a proton motive force across the ICM that is harvested by the ATP synthase to produce ATP.[21] ICMs are often continuous with, but sometimes detached from,[39] the cytoplasmic membrane (CM),[40] just as cristae are continuous with the mitochondrial inner membrane. In *S. cerevisiae* mitochondria, the disruption of Mic60 leads to functional defects such as decreased growth rate under respiratory conditions (i.e., non-fermentable media).[41,42] If Mic60 is involved in the development of photosynthetic ICMs, then its disruption should lead to growth defects in the absence of oxygen and the presence of light.

To assess whether Mic60 and Orf52 have an impact on photoheterotrophic growth and ICM development, we first knocked out these genes in two phylogenetically distant purple alphaproteobacteria amenable to reverse genetics, *R. sphaeroides* and *R. palustris*.[43,44] These knockout strains (Δ*mic60* and Δ*orf52*) were confirmed by PCR, using several sets of internal and external primers that flank the knockout gene construct junctions (Figures S2A and S2B).

Under chemoheterotrophic conditions (i.e., absence of light and presence of oxygen), purple alphaproteobacteria do not develop photosynthetic ICMs for light harvesting. Our data show that there are no growth differences between *mic60*$^+$*orf52*$^+$ wild type (WT) and the Δ*mic60* and Δ*orf52* strains under these conditions (Figure S3A). These bacteria develop a moderate amount of ICMs under anoxia and high light intensity. The Δ*mic60* strain had a slower photoheterotrophic growth rate, relative to WT, in *R. sphaeroides* under this condition (Figures 3C and S4C). The Δ*orf52* strains decreased photoheterotrophic growth significantly, relative to WT, in both alphaproteobacteria (Figures 3A, 3C, S4A, and S4C). Under anoxia and low light intensity, purple alphaproteobacteria upregulate the LH2 complex and develop even larger amounts of ICMs to increase light capturing. As expected, both Δ*mic60* and Δ*orf52* strains displayed slower photoheterotrophic growth rates in both alphaproteobacteria under these more stressful conditions (Figures 3B, 3D, S4B, and S4D). The Δ*mic60* strains had a slower photoheterotrophic growth rate, relative to WT, in both alphaproteobacteria, whereas the Δ*orf52* strain grew significantly slower than WT only in *R. palustris*. Interestingly, Δ*orf52* displayed much more severe decreases in growth rate and yield than Δ*mic60* in *R. palustris*, which is opposite from what was observed in *R. sphaeroides*. This indicates that these proteins might contribute differently to photoheterotrophic growth in these two distantly related species. In summary, the slower photoheterotrophic growth rate of the knockout strains, especially when more ICMs are required, suggests that Mic60 and Orf52 affect the development of photosynthetic ICMs.

Mic60 and Orf52 are involved in the formation of lamellar and vesicular ICMs

The disruption of mitochondrial Mic60 leads to structural defects such as the loss of crista junctions, detachment of cristae from the mitochondrial envelope, and elongated crista membranes.[17,45] Hypotheses about the role of Mic60 in ICM development postulate that this protein might be responsible for creating ICM junctions and contact sites that respectively compartmentalize ICMs and anchor them to the bacterial envelope.[25] The loss and overexpression of Mic60 and Orf52 from ICM-developing alphaproteobacteria might thus lead to ICM morphology defects.

To directly address whether the gene products of *mic60* and *orf52* are involved in ICM formation, we generated *R. palustris* and *R. sphaeroides* strains capable of overexpressing Mic60 and Orf52 (Mic60↑ and Orf52↑, respectively). These strains were verified by reverse-transcriptase quantitative PCR upon 6-h induction with 1 mM isopropyl-β-D-thiogalactoside (IPTG). Both Mic60↑ and Orf52↑ strains had an increase in gene expression of ∼7- to 9-fold in *R. sphaeroides*, and of about 2-fold in *R. palustris*, relative to ex-conjugants grown without IPTG (Figure S2C). The knockout and WT strains plus overexpression ex-conjugants were grown under photoheterotrophic conditions

Please cite this article in press as: Muñoz-Gómez et al., Intracytoplasmic-membrane development in alphaproteobacteria involves the homolog of the mitochondrial crista-developing protein Mic60, Current Biology (2023), https://doi.org/10.1016/j.cub.2023.02.059

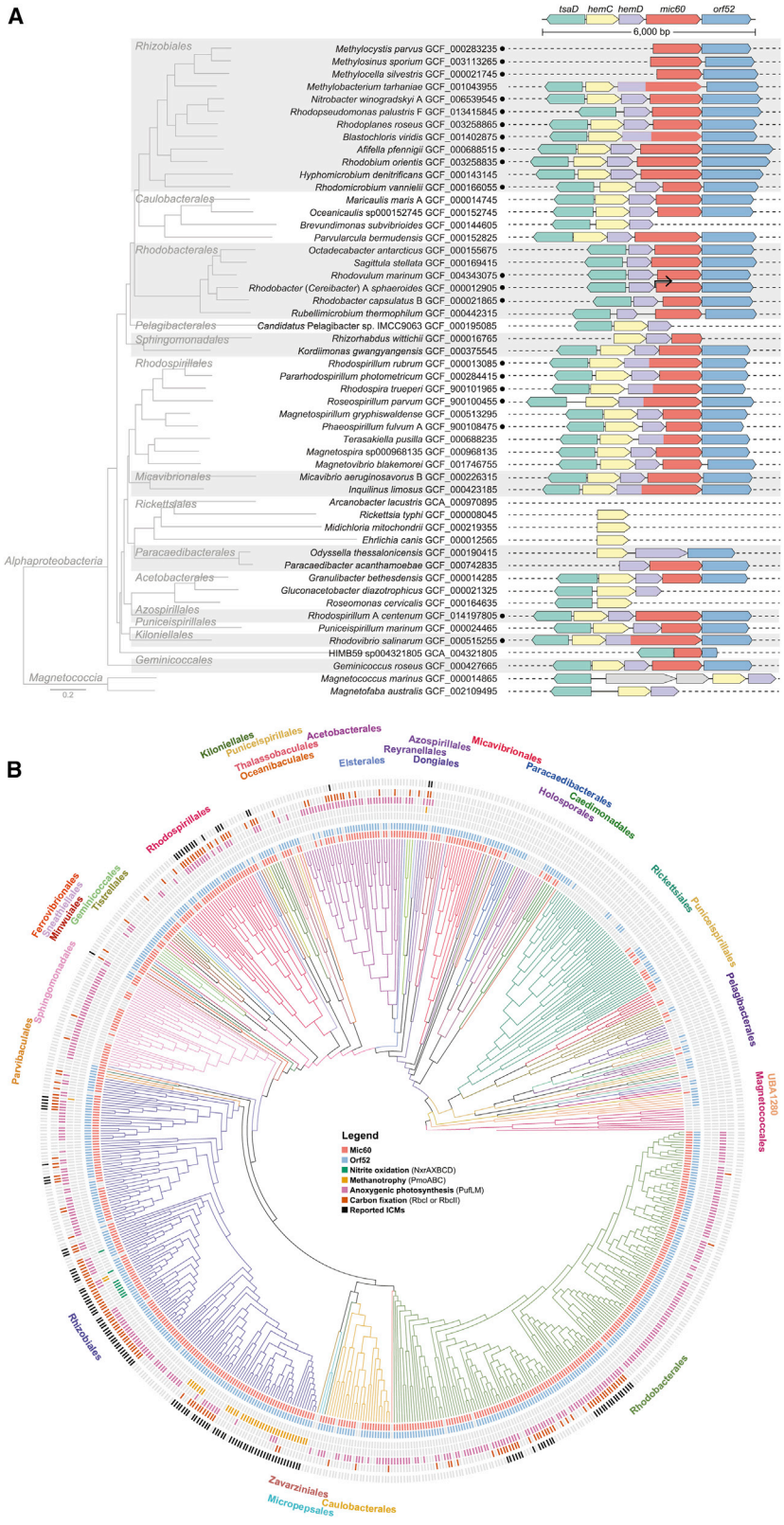

Figure 2. Evolutionary conservation of the secondary and tertiary structure of mitochondrial and alphaproteobacterial Mic60

(A) Alignment of C-terminal signature mitofilin domain and its adjacent N-terminal region of representative alphaproteobacteria and eukaryotes. This alignment has the Mic60 amino acid sequence of *R. sphaeroides* as a reference and was obtained from JPred4.[34] The amino acid colors are based on physicochemical properties, and color intensity reflects evolutionary conservation of the site in the alignment. The red arrow points to the conserved Phe327 in the *R. sphaeroides* Mic60 homolog. Common gaps are hidden from the alignment as per JPred4 output.

(B and C) Helical wheel projection of the amphipathic helix that comprises LBS1 in *R. palustris* (B) and *R. sphaeroides* (C), as predicted by the HELIQUEST web server.[35]

(D and E) Structural alignments of the C-terminal region of Mic60 homologs from the eukaryote *L. thermotolerans* (yellow) and the bacteria (pink) *R. palustris* (D) or *R. sphaeroides* (E). Figure S1 shows AlphaFold2 structure predictions for entire protein sequences.

See also Figure S1.

Please cite this article in press as: Muñoz-Gómez et al., Intracytoplasmic-membrane development in alphaproteobacteria involves the homolog of the mitochondrial crista-developing protein Mic60, Current Biology (2023), https://doi.org/10.1016/j.cub.2023.02.059

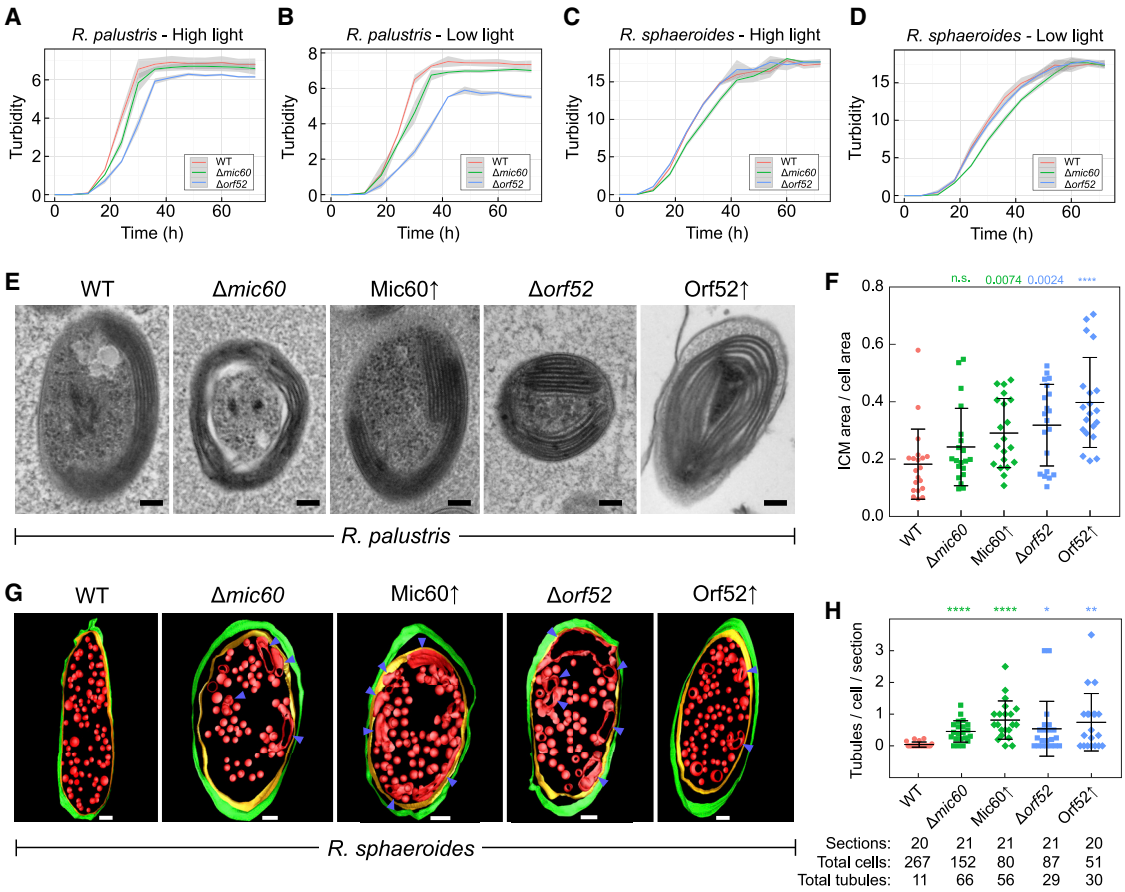

Figure 3. The disruption of the *mic60* and *orf52* genes causes defects in photoheterotrophic growth and ICM development

(A–D) Growth curves of *R. palustris* WT and Δ*mic60* and Δ*orf52* strains under high (A) and low (B) light, and *R. sphaeroides* under high (C) and low (D) light. Gray areas surrounding growth curves depict the standard deviation around the mean for three biological replicates.

(E) Exemplar TEM micrographs of each *R. palustris* strain grown in low light.

(F) Column scatterplot of the ratio of *R. palustris* ICM area/whole-cell area (y axis) measured from 20 cells imaged using TEM in *R. palustris* WT, knockout (Δ*mic60* and Δ*orf52*), and overexpression (Mic60↑ and Orf52↑) strains. Mean and standard deviation shown by middle bar and whiskers, respectively. Values and asterisks above each column represent statistical significance of the difference of each population compared with WT.

(G) Exemplar electron tomograms of each *R. sphaeroides* strain grown in low light. Blue arrows point at aberrant ICMs.

(H) Column scatterplot of tubules/cell per section (y axis) for *R. sphaeroides* WT, knockout (Δ*mic60* and Δ*orf52*), and overexpression (Mic60↑ and Orf52↑) strains. The number of sections, cells, and tubules for each cell line is given in the table below, the x axis. Mean and standard deviation shown by middle bar and whiskers, respectively. Asterisks above each column represent statistical significance of the difference of each mutant population compared with WT. Related to Video S1. Scale bars, 100 nm (E and G). Statistical significance: *p < 0.05; **p < 0.01; ***p < 0.001; ****p < 0.0001.

See also Figures S2–S5.

and low light to maximize ICM development. The strains were imaged using transmission electron microscopy (TEM), and randomized micrographs were blindly scored to quantitatively evaluate peripheral stacked lamellae in *R. palustris* and uniformly distributed vesicles in *R. sphaeroides*[23] (Figures 3E–3H; Video S1).

In *R. palustris*, the area occupied by lamellar ICMs increased relative to the whole-cell area in both knockout (Δ*mic60* and Δ*orf52*) and overexpression (Mic60↑ and Orf52↑) strains, as compared with WT (mean ratio ICM area/cell area = 0.18 ± 0.03) (Figures 3E and 3F). This increase was statistically significant in Mic60↑ (0.29 ± 0.03) but not in Δ*mic60* (0.24 ± 0.03). Both Δ*orf52* (0.32 ± 0.03) and Orf52↑ (0.40 ± 0.04) demonstrated higher and statistically significant increases in ICM:cell area ratios, compared with their Mic60 counterparts. In *R. sphaeroides*, we scored for the appearance of elongated ICMs (i.e., tubules) per cell as these were rarely observed in the WT strain (tubules/cell/section = 0.04 ± 0.02) (Figures 3G and 3H). Both Δ*mic60* (0.46 ± 0.07) and Mic60↑ (0.82 ± 0.13) showed a highly statistically significant increase in the number of tubules, whereas they were observed to a lesser extent in Δ*orf52* (0.54 ± 0.19) and Orf52↑ (0.74 ± 0.20). Moreover, among tubulated ICMs, Mic60↑ displayed a significantly higher incidence of branching ICMs, relative to Δ*mic60* (Figure S5), reminiscent of the branched cristae seen in *S. cerevisiae MIC60*↑.[45] Electron tomograms were used to render representative images of *R. sphaeroides* cells whose ICM membranes were not well contrasted (Figure 3G; Video S1). This revealed the presence of elongated ICMs of various lengths and volumes in all the mutant strains assayed.

Please cite this article in press as: Muñoz-Gómez et al., Intracytoplasmic-membrane development in alphaproteobacteria involves the homolog of the mitochondrial crista-developing protein Mic60, Current Biology (2023), https://doi.org/10.1016/j.cub.2023.02.059

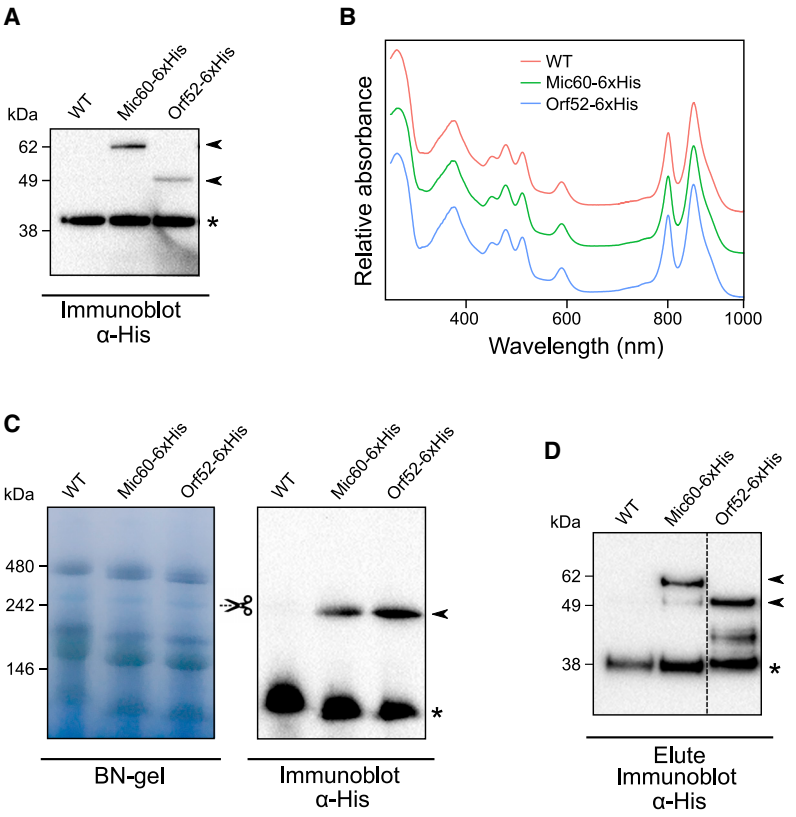

Figure 4. Mic60 and Orf52 assemble into a 250 kDa protein complex in *R. sphaeroides*

(A) Immunoblot verifying the expression of Mic60-6xHis and Orf52-6xHis.

(B) Absorption spectra (x axis) of ICMs isolated from Mic60-6xHis, Orf52-6xHis, and WT control strains. Relative absorbance given on y axis, and spectra are normalized to the bacteriochlorophyll *a* Qx peak at 590 nm. Stacked spectra are color-coded according to the legend (upper right-hand corner).

(C) Protein complexes from detergent-solubilized isolated ICMs resolved by BN-PAGE. Scissor symbol indicates the ~250 kDa band excised for MS analysis (see Figure S6A and Data S1). Right gel shows immunoblot demonstrating that Mic60-6xHis and Orf52-6xHis assemble into a ~250 kDa band.

(D) Immunoblot of Mic60-6xHis and Orf52-6xHis affinity-purification eluates showing these baits were successfully purified from detergent-solubilized isolated ICMs. Molecular weight markers shown to left of gels. Arrowheads point to specific His antibody signals absent in WT controls; asterisks denote non-specific band used as loading control.

The ultrastructural defects of the Δ*mic60* and Δ*orf52* strains of *R. sphaeroides* and *R. palustris* are consistent with their lower photoheterotrophic growth dynamics. Namely, the Δ*orf52* strain exhibits more pronounced phenotypes than the Δ*mic60* strains in *R. palustris*, whereas the opposite is true in *R. sphaeroides*. These defects in ICM area and shape were not paralleled by the absorbance spectra of whole cells, suggesting the regulation of RC-LH1 and LH2 complexes is largely unaffected (Figures S3B and S3C). We also observed that both knockout and overexpression strains exhibited ICM area expansion. It is possible that both conditions lead to unregulated membrane growth that produce seemingly similar phenotypes under the image analyses employed here. However, improved sample preservation and larger-scale volumetric electron microscopy will be required to quantitatively assess changes in the shape and number of ICM junctions, which potentially differ between knockout and overexpression strains. The expansion of photosynthetic ICMs is similar to the enlarged respiratory cristae observed in *S. cerevisiae* and *T. brucei* mitochondria defective of Mic60, as well as to the enlarged magnetosomes reported in the magnetotactic alphaproteobacterium *M. gryphiswaldense* upon deletion of the *mic60* paralog. Together, the ultrastructural defects displayed by both Δ*mic60* and Δ*orf52* suggest that these genes are involved in photosynthetic ICM development.

Mic60 and Orf52 are assembled into a 250 kDa complex in the ICMs of *R. sphaeroides*

Eukaryotic MICOS comprises 6–9 subunits in *H. sapiens*, *S. cerevisiae*, and *T. brucei*. Four of them—Mic60, Mic10, Mic19, and Mic12—are inferred to be ancestral to eukaryotes.[18,19] Furthermore, MICOS has been suggested to engage in interactions with a myriad of other proteins, such as the outer membrane (OM) β-barrel insertase Sam50, the OM translocase Tom40, and the mitochondrial intermembrane space assembly protein Mia40.[12,46] It is thus possible that alphaproteobacterial Mic60 and Orf52 are part of a larger multi-protein complex at alphaproteobacterial envelopes.

To investigate this hypothesis, *R. sphaeroides* was transformed to allow IPTG-inducible expression of either Mic60 or Orf52 bearing a C-terminal hexa-histidine (6xHis) tag. Upon successfully verifying Mic60-6xHis and Orf52-6xHis expression (Figure 4A), we noticed the former migrated at ~62 kDa, in contrast to its theoretical 43.8 kDa molecular weight, which is likely explained by the anomalous mobility of acidic proteins in SDS-PAGE.[47] ICMs (i.e., chromatophores) were isolated from the two overexpression strains alongside the WT control. The absorption spectra of the isolated ICMs from each strain were essentially identical, indicating that Mic60-6xHis and Orf52-6xHis overexpression does not affect the RC-LH1:LH2 protein composition ratio of ICMs (Figure 4B).

The isolated ICMs were resolved by blue native PAGE (BN-PAGE) gels and transferred onto a membrane for probing with anti-His antibody (Figure 4C). Both Mic60-6xHis and Orf52-6xHis incorporate into a ~250 kDa multi-protein complex; the antibody signal was absent in WT. Notably, the immunoreactive ~250-kDa-sized band seems to correspond to a faint and similarly sized Coomassie-stained band in the BN-PAGE gel. To identify proteins migrating here, four ~250 kDa bands were excised from *R. sphaeroides* WT, and the eluted proteins were analyzed by liquid chromatography-tandem mass spectroscopy (LC-MS/MS) (Figure S6A). Mic60 and Orf52 were found among the 175 top proteins in the ~250 kDa band with a mean intensity score >23 from all biological replicates (Data S1). The top three hits corresponded to RC complex subunits H, M, and L,

Please cite this article in press as: Muñoz-Gómez et al., Intracytoplasmic-membrane development in alphaproteobacteria involves the homolog of the mitochondrial crista-developing protein Mic60, Current Biology (2023), https://doi.org/10.1016/j.cub.2023.02.059

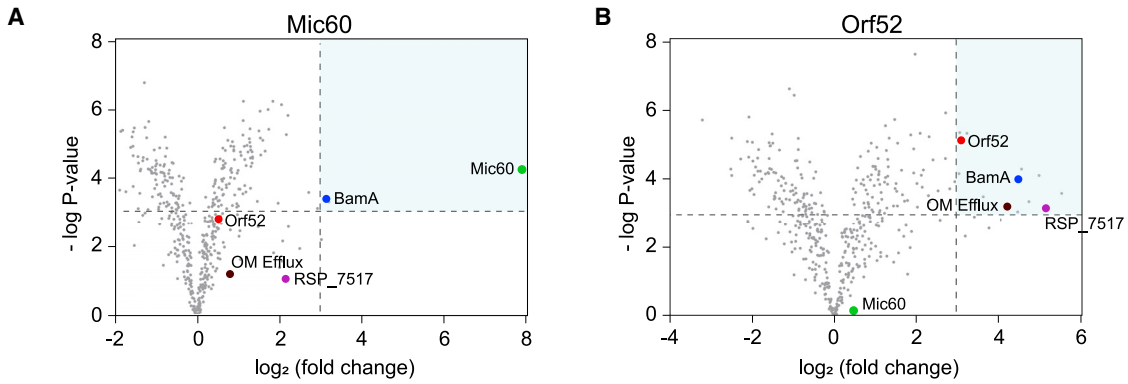

C

Mic60 interactors

Protein	Fold change	UPB	ICM	250 kDa complex	Weight (kDa)
Mic60 (Mitofilin)	245.13	○	○*	●	43.8
BamA	9.09	●	●	●	88.2

D

Orf52 interactors

Protein	Fold change	UPB	ICM	250 kDa complex	Weight (kDa)
RSP_7517	35.62	○	○	◉	4.8
BamA	22.38	●	●	●	88.2
OM Efflux protein	18.52	●	●	●	49.7
Orf52 (Tetratricopeptide repeat (TPR))	8.50	●	●	●	52.5

β-barrel, POTRA, TMD

Figure 5. Mic60 and Orf52 interactomes demonstrate that both proteins interact with the outer membrane β-barrel protein BamA in *R. sphaeroides*

(A and B) Volcano plots of proteins identified by MS in Mic60-6xHis (A) and Orf52-6xHis (B) AP eluates, with −log p values for each protein (y axis) plotted against $\log_2$-tranformed fold-enrichment over WT negative control (x axis); >3 thresholds for each value are indicated by dotted lines and blue shading. Baits and enriched interactors are indicated by labeled, colored dots, whereas other proteins are depicted in gray.

(C and D) Summary of enriched interactors found in Mic60-6xHis (C) and Orf52-6xHis (D) APs, using the volcano plot color scheme. Left of protein names: domain architecture schemas, fold change in APs versus negative controls, presence in UPB and ICM proteomes,[49] presence in ∼250 kDa band proteome (Data S1), and theoretical molecular (Mol.) weight. Black dots indicate presence in proteome; gray dot indicates presence below our defined threshold; *, presence in ICM according to a previous MS analysis.[48]

See also Figure S6 and Data S2.

which were previously shown to co-migrate with Mic60 in BN-PAGE.[48] These data are consistent with previous detection of Mic60 and Orf52 in isolated ICMs and in their developmental precursors called "upper pigmented bands" (UPBs).[48,49] These experiments thus show that Mic60 and Orf52 are part of a higher-order assembly complex of ∼250 kDa present in photosynthetic ICMs.

Mic60 and Orf52 interact with the OM β-barrel insertase BamA

Among several interactions reported for eukaryotic MICOS, the Mic60-Sam50 interaction was suggested to have predated the origin of mitochondria.[46] This interaction is required for making contact sites at the mitochondrial envelope of phylogenetically disparate eukaryotes such as *H. sapiens*, *S. cerevisiae*, and *T. brucei*.[14,15,17] Furthermore, the bacterial homolog of Sam50, BamA, is a ubiquitous protein of bacteria surrounded by two membranes that is required for the assembly of β-barrels into the OM.[50–52] These observations and inferences prompted us to next investigate potential physical interactors of alphaproteobacterial Mic60 (YP_351551.1) and Orf52 (YP_351550.1).

Affinity purification (AP) of Mic60-6xHis and Orf52-6xHis was performed on isolated ICMs from *R. sphaeroides* solubilized with a mixture of non-ionic detergents. The successful capture of Mic60-6xHis and Orf52-6xHis by cobalt-coated Dynabeads was confirmed (Figure 4D); a mock AP was done on WT as a control for non-specific binding. Beads from triplicate APs of Mic60-6xHis, Orf52-6xHis, and mock control were trypsinized and analyzed by LC-MS/MS. Protein enrichment in bait-APs in comparison with the mock control was quantified using label-free quantification as previously described.[53] In each AP, 497 high-confidence proteins were found (Data S2) based on mean Andromeda confidence scores >100 in three biological replicates.[54] The criteria for true interactors among these proteins were as follows: (1) $\log_2$-transformed fold-enrichment and p values > 3 (Figures 5A and 5B), (2) being part of the aforementioned ∼250 kDa complex (Data S1), (3) previously reported in ICM and/or UPBs (Figures 5C and 5D), and (4) predicted transmembrane segments or a β-barrel structure (Figures 5C and 5D).

The data show that both Mic60-6xHis and Orf52-6xHis interact with BamA (Figures 5 and S6A–S6C). Somewhat unexpectedly, Mic60-6xHis and Orf52-6xHis do not interact with

Please cite this article in press as: Muñoz-Gómez et al., Intracytoplasmic-membrane development in alphaproteobacteria involves the homolog of the mitochondrial crista-developing protein Mic60, Current Biology (2023), https://doi.org/10.1016/j.cub.2023.02.059

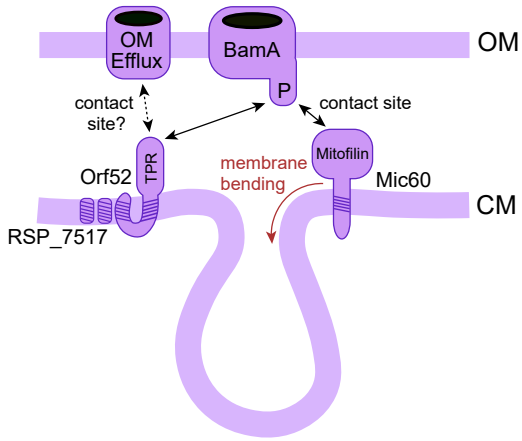

Figure 6. Summary of physical interactions hypothesized to underpin contact site and ICM junction formation at an alphaproteobacterial envelope

Model based on the physical Mic60 interactors reported for *R. sphaeroides* in this study and shown in Figure 5. Red arrow indicates demonstrated *in vitro* membrane-remodeling activity of alphaproteobacterial Mic60.[26] CM, cytoplasmic membrane; OM, outer membrane.

each other, as neither protein was found to co-purify with either bait (Figures 5A–5D). We cannot exclude that the C-terminal 6x-His tag may have interfered with their interaction, although its small size likely precludes this possibility. Mic60 was also not found to interact with HemD, although these proteins have fused in some alphaproteobacteria (Figure 2A).[19] However, this was expected as the HemD-Mic60 fusion is predicted to be membrane-anchored at its midpoint, with the HemD and Mic60 fragments exposed to the cytoplasm and periplasm, respectively. Moreover, the high degree of Mic60 enrichment relative to BamA (Figures 5B and 5D) is consistent with the idea that Mic60 forms homo-oligomers, as demonstrated for its eukaryotic counterparts.[33,36,41]

In contrast to Mic60, Orf52 interacts with a β-barrel protein annotated as OM efflux (OM Efflux) and a very small 4.8 kDa protein with an N-terminal TMD that is encoded by the RSP_7517 locus (Figures 5A and 5D). Interestingly, the former was found to be more abundant in ICMs than the UBP precursor.[49] The enrichment of RSP_7515 is surprising as it was not previously detected in ICMs or UPBs.[49] It was, however, detected in the ~250 kDa BN-PAGE band, albeit below our defined threshold by a single peptide (Data S1). This may be explained by RSP_7517 yielding only two trypsin peptides that are highly hydrophobic, making it less amenable for the shotgun LC-MS/MS detection employed on the 250 kDa complex[55] (Figure S6D). In conclusion, the Sam50 homolog BamA appears to be the only physical interactor of alphaproteobacterial Mic60 (Figure 5E), and this interaction has been conserved despite ~2 billion years of evolutionary divergence of modern alphaproteobacteria from mitochondria.

DISCUSSION

Our overarching aim was to empirically investigate alphaproteobacterial Mic60, thereby testing the hypothesis that ICMs were transformed into cristae during the early evolution of mitochondria.[25] To this end, we focused on two distantly related purple alphaproteobacteria, *R. palustris* and *R. sphaeroides*. We showed that alphaproteobacterial Mic60 (1) has a conserved predicted tertiary structure and membrane-bending amphipathic helix, (2) affects photoheterotrophic growth and ICM development and shape, (3) is part of a higher-order multi-protein complex in photosynthetic ICMs, and (4) most likely interacts with the core BamA subunit of the OM BAM complex. Furthermore, we also showed that Orf52, encoded by a *mic60*-adjacent gene in alphaproteobacteria (but with no homologs in eukaryotes), also shares these features despite not interacting with Mic60.

These findings are consistent with previous observations that also support a functional conservation of Mic60 and its involvement in ICM development. First, the expression profile of Mic60 follows photosynthetic ICM development in the absence of oxygen and presence of light.[56] Second, Mic60 localizes to photosynthetic ICMs in three phylogenetically disparate alphaproteobacteria, *R. sphaeroides* (*Rhodobacterales*), *Rhodospirillum rubrum* (*Rhodospirillales*), and *R. palustris* (*Rhizobiales*), as demonstrated by proteomic characterization of isolated ICMs.[48,49,57,58] Third, *R. sphaeroides* Mic60 is capable of binding and tubulating membranes *in vitro*, and its heterologous overexpression induces ICM-like structures in *E. coli*.[26] Fourth, disruption of *mic60* and *orf52* paralogs in the alphaproteobacterial genus *Magnetospirillum*[18] leads to fewer and larger magnetosomes.[59,60] Multiple sources of evidence thus support the notion that Mic60 function has been conserved in alphaproteobacteria and mitochondria.

What is the precise role of Mic60 in ICM development? Mic60 likely introduces curvature at ICM junctions through an amphipathic helix that is conserved between mitochondria and alphaproteobacteria. We show that alphaproteobacterial Mic60 most likely interacts with BamA, the homolog of Sam50. In mitochondria, Sam50 interacts with Mic60 through its intermembrane space-protruding POTRA domains, and it is likely that the same type of interaction occurs in the periplasm of alphaproteobacteria. This ancient protein-protein interaction suggests that in addition to aiding ICM junction formation, alphaproteobacterial Mic60 is also involved in the formation of contact sites that may help to stabilize ICMs by providing an OM anchor for high membrane curvature at ICM junctions (Figure 6).[61] The formation of crista junctions and contact sites by Mic60 is aided by Mic19 in mitochondria,[33,36] but there is no evidence for a Mic19-like protein in alphaproteobacteria; our pull-downs did not reveal proteins with typical Mic19 motifs. In summary, it appears that both the formation of contact sites and crista/ICM junctions have been conserved in alphaproteobacteria and mitochondria (Figure 6).

The larger macromolecular complex that Mic60 is part of in *R. sphaeroides* is reminiscent of the extended ER-mitochondria interaction network named ERMIONE, which is organized around the interaction of Mic60 with the OM SAM and TOM complexes.[62] In yeast, ERMIONE plays a major role in mitochondrial biogenesis by connecting the ER-mitochondria encounter structure (ERMES) to MICOS.[10,62] In humans, MICOS and SAM interact stably to form the mitochondrial intermembrane space bridging complex.[63] It is possible that BamA, through its interactions with Mic60, Orf52, OM Efflux, and RSP_7515, serves as the

hub of a larger protein-interaction network. In the model alphaproteobacterium *Caulobacter crescentus*, the BAM complex has been shown to have a modular structure, including a ~300 kDa subcomplex,[64,65] which is reminiscent of the Mic60/Orf52-containing complex observed here.

The evidence for the structural and functional conservation of alphaproteobacterial Mic60 relative to its mitochondrial homolog is most compatible with an evolutionary scenario in which ICMs and cristae are homologous. This implies that cristae most likely evolved from the ICMs developed by the last common ancestor of mitochondria and its sister group, the *Alphaproteobacteria*; cristae thus have a pre-endosymbiotic origin. If this hypothesis turns out to be correct, bioenergetic ICMs might have pre-adapted the first mitochondrial ancestor to become an efficient bioenergetic or respiratory organelle.[25] The widespread but sporadic phylogenetic distribution of ICMs across the *Alphaproteobacteria* is then most likely explained by multiple independent losses. This is conceivable as both cristae and ICMs are known to have been lost repeatedly as a result of physiological specialization to different environments (e.g., transitions to anaerobiosis in mitochondria or to heterotrophy in photosynthetic bacteria). Nevertheless, some Mic60-bearing alphaproteobacteria do not appear to develop ICMs. In the absence of ICM formation, Mic60 may mediate other important functions, like contact site formation via BamA interaction for lipid transfer or protein export. This more general function might have been ancestral to Mic60 and agrees with the observation that a distant homolog of Mic60 that lacks the conserved C-terminal mitofilin domain, namely HemX, is restricted to and widespread in the *Gammaproteobacteria*.[19] It is thus conceivable that the mitofilin domain first evolved in a HemX-like protein and that this coincided with the origin of ICMs in a common ancestor of alphaproteobacteria and mitochondria.

Future studies are required to mechanistically elucidate how alphaproteobacterial Mic60 interacts with BamA and to determine whether alphaproteobacterial Mic60 forms homotetramers as recently reported for fungal Mic60.[36] More generally, efforts focused on phylogenetically disparate alphaproteobacteria with and without ICMs will shed light on the functions and mechanisms of Mic60 in prokaryotes. Altogether, the structural and functional conservation of alphaproteobacterial Mic60 shown here suggests a role in curving membranes at ICM junctions and making contact sites at envelopes. It is therefore probable that the mitochondrial ancestor was an ICM-bearing alphaproteobacterium.

STAR★METHODS

Detailed methods are provided in the online version of this paper and include the following:

- KEY RESOURCES TABLE
- RESOURCE AVAILABILITY
  - Lead contact
  - Materials availability
  - Data and code availability
- EXPERIMENTAL MODEL AND SUBJECT DETAILS
  - Bacterial strains, media, and growth conditions
- METHOD DETAILS
  - Bioinformatic analysis
  - DNA methods and plasmid construction
  - Construction of *R. sphaeroides* and *R. palustris* knockout strains
  - Construction of *R. sphaeroides* and *R. palustris* overexpression strains
  - RT qPCR
  - Transmission electron microscopy
  - SDS PAGE and Western blotting
  - Isolation of ICMs via high-pressure homogenization and light spectroscopy
  - Blue Native PAGE
  - Affinity purification
  - Protein preparation and mass spectroscopy
  - Analysis of mass spectroscopy peptides
- QUANTIFICATION AND STATISTICAL ANALYSIS

SUPPLEMENTAL INFORMATION

Supplemental information can be found online at https://doi.org/10.1016/j.cub.2023.02.059.

ACKNOWLEDGMENTS

We dedicate this work to Thomas Cavalier-Smith, whose large-scale synthetic work on evolutionary cell biology stimulated thinking on this topic by S.A.M.-G. many years ago. We thank Karel Harant and Pavel Talacko (Charles University, Prague) for performing LC-MS analysis and Michala Boudová (Center Algatech) for technical assistance. S.A.M.-G. is supported by an EMBO Postdoctoral Fellowship (ALTF 21-2020). M.M.L. was supported by a Nova Scotia Health Research Foundation (NSHRF) Scotia Scholarship 2012-8781. This work was also supported by the Czech Science Foundation grants 20-23513S to H.H. and 19-28778X to M.K., the ERD Fund (003/0000441) to T.B., as well as the Czech Ministry of Education grant OPVVV16_019/0000759 to J.L. and Czech BioImaging grant LM2015062. A.J.R. and J.T.B. were supported by the Natural Sciences and Engineering Research Council of Canada (grants RGPIN-2022-05430 and RGPIN-2018-08398, respectively).

AUTHOR CONTRIBUTIONS

S.A.M.-G., L.R.C., and H.H. designed the research; S.A.M.-G., L.R.C., A.T.G., M.M.L., S.S., L.B.C., T.B., K.K., J.T.B., and H.H. conducted the research; S.A.M.-G., L.R.C., A.T.G., S.S., T.B., and H.H. analyzed the data; S.A.M.-G., L.R.C., A.T.G., M.K., J.L., and H.H. wrote the paper; and J.T.B., M.K., A.J.R., C.H.S., J.L., and H.H. acquired the funding.

DECLARATION OF INTERESTS

The authors declare no competing interests.

Received: November 6, 2022
Revised: February 6, 2023
Accepted: February 16, 2023
Published: March 14, 2023

REFERENCES

1. Roger, A.J., Muñoz-Gómez, S.A., and Kamikawa, R. (2017). The origin and diversification of mitochondria. Curr. Biol. *27*, R1177–R1192. https://doi.org/10.1016/j.cub.2017.09.015.
2. Muñoz-Gómez, S.A., Susko, E., Williamson, K., Eme, L., Slamovits, C.H., Moreira, D., López-García, P., and Roger, A.J. (2022). Site-and-branch-heterogeneous analyses of an expanded dataset favour mitochondria as sister to known Alphaproteobacteria. Nat. Ecol. Evol. *6*, 253–262. https://doi.org/10.1038/s41559-021-01638-2.

3. Martijn, J., Vosseberg, J., Guy, L., Offre, P., and Ettema, T.J.G. (2018). Deep mitochondrial origin outside the sampled Alphaproteobacteria. Nature *557*, 101–105. https://doi.org/10.1038/s41586-018-0059-5.

4. Fan, L., Wu, D., Goremykin, V., Xiao, J., Xu, Y., Garg, S., Zhang, C., Martin, W.F., and Zhu, R. (2020). Phylogenetic analyses with systematic taxon sampling show that mitochondria branch within Alphaproteobacteria. Nat. Ecol. Evol. *4*, 1213–1219. https://doi.org/10.1038/s41559-020-1239-x.

5. Schavemaker, P.E., and Muñoz-Gómez, S.A. (2022). The role of mitochondrial energetics in the origin and diversification of eukaryotes. Preprint at bioRxiv. https://doi.org/10.1101/2021.10.23.465364.

6. Daems, W.T., and Wisse, E. (1966). Shape and attachment of the cristae mitochondriales in mouse hepatic cell mitochondria. J. Ultrastruct. Res. *16*, 123–140. https://doi.org/10.1016/s0022-5320(66)80027-8.

7. Mannella, C.A., Marko, M., Penczek, P., Barnard, D., and Frank, J. (1994). The internal compartmentation of rat-liver mitochondria: tomographic study using the high-voltage transmission electron microscope. Microsc. Res. Tech. *27*, 278–283. https://doi.org/10.1002/jemt.1070270403.

8. Perkins, G., Renken, C., Martone, M.E., Young, S.J., Ellisman, M., and Frey, T. (1997). Electron tomography of neuronal mitochondria: three-dimensional structure and organization of cristae and membrane contacts. J. Struct. Biol. *119*, 260–272. https://doi.org/10.1006/jsbi.1997.3885.

9. Zick, M., Rabl, R., and Reichert, A.S. (2009). Cristae formation-linking ultrastructure and function of mitochondria. Biochim. Biophys. Acta *1793*, 5–19. https://doi.org/10.1016/j.bbamcr.2008.06.013.

10. Wideman, J.G., and Muñoz-Gómez, S.A. (2016). The evolution of ERMIONE in mitochondrial biogenesis and lipid homeostasis: an evolutionary view from comparative cell biology. Biochim. Biophys. Acta *1861*, 900–912. https://doi.org/10.1016/j.bbalip.2016.01.015.

11. Kühlbrandt, W. (2019). Structure and mechanisms of F-type ATP synthases. Annu. Rev. Biochem. *88*, 515–549. https://doi.org/10.1146/annurev-biochem-013118-110903.

12. Pánek, T., Eliáš, M., Vancová, M., Lukeš, J., and Hashimi, H. (2020). Returning to the fold for lessons in mitochondrial crista diversity and evolution. Curr. Biol. *30*, R575–R588. https://doi.org/10.1016/j.cub.2020.02.053.

13. Rampelt, H., Zerbes, R.M., van der Laan, M., and Pfanner, N. (2017). Role of the mitochondrial contact site and cristae organizing system in membrane architecture and dynamics. Biochim. Biophys. Acta Mol. Cell Res. *1864*, 737–746. https://doi.org/10.1016/j.bbamcr.2016.05.020.

14. Kozjak-Pavlovic, V. (2017). The MICOS complex of human mitochondria. Cell Tissue Res. *367*, 83–93. https://doi.org/10.1007/s00441-016-2433-7.

15. Wollweber, F., von der Malsburg, K., and van der Laan, M. (2017). Mitochondrial contact site and cristae organizing system: a central player in membrane shaping and crosstalk. Biochim. Biophys. Acta Mol. Cell Res. *1864*, 1481–1489. https://doi.org/10.1016/j.bbamcr.2017.05.004.

16. Michaud, M., Gros, V., Tardif, M., Brugière, S., Ferro, M., Prinz, W.A., Toulmay, A., Mathur, J., Wozny, M., Falconet, D., et al. (2016). AtMic60 is involved in plant mitochondria lipid trafficking and is part of a large complex. Curr. Biol. *26*, 627–639. https://doi.org/10.1016/j.cub.2016.01.011.

17. Kaurov, I., Vancová, M., Schimanski, B., Cadena, L.R., Heller, J., Bílý, T., Potěšil, D., Eichenberger, C., Bruce, H., Oeljeklaus, S., et al. (2018). The diverged trypanosome MICOS complex as a hub for mitochondrial cristae shaping and protein import. Curr. Biol. *28*, 3393–3407.e5. https://doi.org/10.1016/j.cub.2018.09.008.

18. Muñoz-Gómez, S.A., Slamovits, C.H., Dacks, J.B., Baier, K.A., Spencer, K.D., and Wideman, J.G. (2015). Ancient homology of the mitochondrial contact site and cristae organizing system points to an endosymbiotic origin of mitochondrial cristae. Curr. Biol. *25*, 1489–1495. https://doi.org/10.1016/j.cub.2015.04.006.

19. Huynen, M.A., Mühlmeister, M., Gotthardt, K., Guerrero-Castillo, S., and Brandt, U. (2016). Evolution and structural organization of the mitochondrial contact site (MICOS) complex and the mitochondrial intermembrane space bridging (MIB) complex. Biochim. Biophys. Acta *1863*, 91–101. https://doi.org/10.1016/j.bbamcr.2015.10.009.

20. Drews, G. (1991). Intracytoplasmic membranes in bacterial cells: organization, function, and biosynthesis. In Prokaryotic Structure and Function: A New Perspective (Cambridge University Press).

21. Niederman, R.A. (2006). Structure, function and formation of bacterial intracytoplasmic membranes. In Complex Intracellular Structures in Prokaryotes Microbiology Monographs, J.M. Shively, ed. (Springer), pp. 193–227. https://doi.org/10.1007/7171_025.

22. Pinevich, A.V. (1997). Intracytoplasmic membrane structures in bacteria. Endocytobiosis Cell Res. *12*, 9–40.

23. LaSarre, B., Kysela, D.T., Stein, B.D., Ducret, A., Brun, Y.V., and McKinlay, J.B. (2018). Restricted localization of photosynthetic intracytoplasmic membranes (ICMs) in multiple genera of purple nonsulfur bacteria. mBio *9*. e00780-e00718. https://doi.org/10.1128/mBio.00780-18.

24. Sener, M., Strumpfer, J., Singharoy, A., Hunter, C.N., and Schulten, K. (2016). Overall energy conversion efficiency of a photosynthetic vesicle. eLife *5*, e09541. https://doi.org/10.7554/eLife.09541.

25. Muñoz-Gómez, S.A., Wideman, J.G., Roger, A.J., and Slamovits, C.H. (2017). The origin of mitochondrial cristae from Alphaproteobacteria. Mol. Biol. Evol. *34*, 943–956. https://doi.org/10.1093/molbev/msw298.

26. Tarasenko, D., Barbot, M., Jans, D.C., Kroppen, B., Sadowski, B., Heim, G., Möbius, W., Jakobs, S., and Meinecke, M. (2017). The MICOS component Mic60 displays a conserved membrane-bending activity that is necessary for normal cristae morphology. J. Cell Biol. *216*, 889–899. https://doi.org/10.1083/jcb.201609046.

27. Dietz, J.V., Willoughby, M.M., Piel, R.B., Ross, T.A., Bohovych, I., Addis, H.G., Fox, J.L., Lanzilotta, W.N., Dailey, H.A., Wohlschlegel, J.A., et al. (2021). Mitochondrial contact site and cristae organizing system (MICOS) machinery supports heme biosynthesis by enabling optimal performance of ferrochelatase. Redox Biol. *46*, 102125. https://doi.org/10.1016/j.redox.2021.102125.

28. Kobayashi, K., Masuda, T., Tajima, N., Wada, H., and Sato, N. (2014). Molecular phylogeny and intricate evolutionary history of the three isofunctional enzymes involved in the oxidation of protoporphyrinogen IX. Genome Biol. Evol. *6*, 2141–2155. https://doi.org/10.1093/gbe/evu170.

29. Myers, K.S., Vera, J.M., Lemmer, K.C., Linz, A.M., Landick, R., Noguera, D.R., and Donohue, T.J. (2020). Genome-wide identification of transcription start sites in two Alphaproteobacteria, *Rhodobacter sphaeroides* 2.4.1 and *Novosphingobium aromaticivorans* DSM 12444. Microbiol. Resour. Announc. *9*. e00880-e00820. https://doi.org/10.1128/MRA.00880-20.

30. Dziuba, M., Riese, C.N., Borgert, L., Wittchen, M., Busche, T., Kalinowski, J., Uebe, R., and Schüler, D. (2021). The complex transcriptional landscape of magnetosome gene clusters in *Magnetospirillum gryphiswaldense*. mSystems *6*, e0089321. https://doi.org/10.1128/mSystems.00893-21.

31. Imhoff, J.F., Rahn, T., Künzel, S., and Neulinger, S.C. (2017). Photosynthesis is widely distributed among Proteobacteria as demonstrated by the phylogeny of PufLM reaction center proteins. Front. Microbiol. *8*, 2679. https://doi.org/10.3389/fmicb.2017.02679.

32. Iba, K., Takamiya, K., Toh, Y., and Nishimura, M. (1988). Roles of bacteriochlorophyll and carotenoid synthesis in formation of intracytoplasmic membrane systems and pigment-protein complexes in an aerobic photosynthetic bacterium, Erythrobacter sp. strain OCh114. J. Bacteriol. *170*, 1843–1847. https://doi.org/10.1128/jb.170.4.1843-1847.1988.

33. Hessenberger, M., Zerbes, R.M., Rampelt, H., Kunz, S., Xavier, A.H., Purfürst, B., Lilie, H., Pfanner, N., van der Laan, M., and Daumke, O. (2017). Regulated membrane remodeling by Mic60 controls formation of mitochondrial crista junctions. Nat. Commun. *8*, 15258. https://doi.org/10.1038/ncomms15258.

34. Drozdetskiy, A., Cole, C., Procter, J., and Barton, G.J. (2015). JPred4: a protein secondary structure prediction server. Nucleic Acids Res. *43*, W389–W394. https://doi.org/10.1093/nar/gkv332.

35. Gautier, R., Douguet, D., Antonny, B., and Drin, G. (2008). HELIQUEST: a web server to screen sequences with specific alpha-helical properties. Bioinformatics *24*, 2101–2102. https://doi.org/10.1093/bioinformatics/btn392.

36. Bock-Bierbaum, T., Funck, K., Wollweber, F., Lisicki, E., von der Malsburg, K., von der Malsburg, A., Laborenz, J., Noel, J.K., Hessenberger, M., Jungbluth, S., et al. (2022). Structural insights into crista junction formation by the Mic60-Mic19 complex. Sci. Adv. *8*, eabo4946. https://doi.org/10.1126/sciadv.abo4946.

37. Drews, G., and Golecki, J.R. (2004). Structure, molecular organization, and biosynthesis of membranes of purple bacteria. In Anoxygenic Photosynthetic Bacteria Advances in Photosynthesis and Respiration, R.E. Blankenship, M.T. Madigan, and C.E. Bauer, eds. (Kluwer Academic Publishers), pp. 231–257. https://doi.org/10.1007/0-306-47954-0_12.

38. Greening, C., and Lithgow, T. (2020). Formation and function of bacterial organelles. Nat. Rev. Microbiol. *18*, 677–689. https://doi.org/10.1038/s41579-020-0413-0.

39. Noble, J.M., Lubieniecki, J., Savitzky, B.H., Plitzko, J., Engelhardt, H., Baumeister, W., and Kourkoutis, L.F. (2018). Connectivity of centermost chromatophores in *Rhodobacter sphaeroides* bacteria. Mol. Microbiol. *109*, 812–825. https://doi.org/10.1111/mmi.14077.

40. Scheuring, S., Nevo, R., Liu, L.N., Mangenot, S., Charuvi, D., Boudier, T., Prima, V., Hubert, P., Sturgis, J.N., and Reich, Z. (2014). The architecture of *Rhodobacter sphaeroides* chromatophores. Biochim. Biophys. Acta *1837*, 1263–1270. https://doi.org/10.1016/j.bbabio.2014.03.011.

41. John, G.B., Shang, Y., Li, L., Renken, C., Mannella, C.A., Selker, J.M.L., Rangell, L., Bennett, M.J., and Zha, J. (2005). The mitochondrial inner membrane protein mitofilin controls cristae morphology. Mol. Biol. Cell *16*, 1543–1554. https://doi.org/10.1091/mbc.e04-08-0697.

42. Warnsmann, V., Marschall, L.-M., Meeßen, A.C., Wolters, M., Schürmanns, L., Basoglu, M., Eimer, S., and Osiewacz, H.D. (2022). Disruption of the MICOS complex leads to an aberrant cristae structure and an unexpected, pronounced lifespan extension in *Podospora anserina*. Preprint at bioRxiv. https://doi.org/10.1101/2022.03.21.485166.

43. Jaschke, P.R., Saer, R.G., Noll, S., and Beatty, J.T. (2011). Modification of the genome of *Rhodobacter sphaeroides* and construction of synthetic operons. Methods Enzymol. *497*, 519–538. https://doi.org/10.1016/B978-0-12-385075-1.00023-8.

44. Jiao, Y., and Newman, D.K. (2007). The pio operon is essential for phototrophic Fe(II) oxidation in *Rhodopseudomonas palustris* TIE-1. J. Bacteriol. *189*, 1765–1773. https://doi.org/10.1128/JB.00776-06.

45. Rabl, R., Soubannier, V., Scholz, R., Vogel, F., Mendl, N., Vasiljev-Neumeyer, A., Körner, C., Jagasia, R., Keil, T., Baumeister, W., et al. (2009). Formation of cristae and crista junctions in mitochondria depends on antagonism between Fcj1 and Su e/g. J. Cell Biol. *185*, 1047–1063. https://doi.org/10.1083/jcb.200811099.

46. Muñoz-Gómez, S.A., Slamovits, C.H., Dacks, J.B., and Wideman, J.G. (2015b). The evolution of MICOS: ancestral and derived functions and interactions. Commun. Integr. Biol. *8*, e1094593. https://doi.org/10.1080/19420889.2015.1094593.

47. Guan, Y., Zhu, Q., Huang, D., Zhao, S., Jan Lo, L., and Peng, J. (2015). An equation to estimate the difference between theoretically predicted and SDS PAGE-displayed molecular weights for an acidic peptide. Sci. Rep. *5*, 13370. https://doi.org/10.1038/srep13370.

48. D'Amici, G.M., Rinalducci, S., Murgiano, L., Italiano, F., and Zolla, L. (2010). Oligomeric characterization of the photosynthetic apparatus of *Rhodobacter sphaeroides* R26.1 by nondenaturing electrophoresis methods. J. Proteome Res. *9*, 192–203. https://doi.org/10.1021/pr9005052.

49. Jackson, P.J., Lewis, H.J., Tucker, J.D., Hunter, C.N., and Dickman, M.J. (2012). Quantitative proteomic analysis of intracytoplasmic membrane development in *Rhodobacter sphaeroides*. Mol. Microbiol. *84*, 1062–1078. https://doi.org/10.1111/j.1365-2958.2012.08074.x.

50. Höhr, A.I.C., Lindau, C., Wirth, C., Qiu, J., Stroud, D.A., Kutik, S., Guiard, B., Hunte, C., Becker, T., Pfanner, N., et al. (2018). Membrane protein insertion through a mitochondrial β-barrel gate. Science *359*, eaah6834. https://doi.org/10.1126/science.aah6834.

51. Doyle, M.T., and Bernstein, H.D. (2019). Bacterial outer membrane proteins assemble via asymmetric interactions with the BamA β-barrel. Nat. Commun. *10*, 3358. https://doi.org/10.1038/s41467-019-11230-9.

52. Voulhoux, R., Bos, M.P., Geurtsen, J., Mols, M., and Tommassen, J. (2003). Role of a highly conserved bacterial protein in outer membrane protein assembly. Science *299*, 262–265. https://doi.org/10.1126/science.1078973.

53. Cadena, L.R., Gahura, O., Panicucci, B., Zíková, A., and Hashimi, H. (2021). Mitochondrial contact site and cristae organization system and F_1F_O-ATP synthase crosstalk is a fundamental property of mitochondrial cristae. mSphere *6*, e0032721. https://doi.org/10.1128/mSphere.00327-21.

54. Cox, J., Neuhauser, N., Michalski, A., Scheltema, R.A., Olsen, J.V., and Mann, M. (2011). Andromeda: a peptide search engine integrated into the MaxQuant environment. J. Proteome Res. *10*, 1794–1805. https://doi.org/10.1021/pr101065j.

55. Barrera, N.P., and Robinson, C.V. (2011). Advances in the mass spectrometry of membrane proteins: from individual proteins to intact complexes. Annu. Rev. Biochem. *80*, 247–271. https://doi.org/10.1146/annurev-biochem-062309-093307.

56. Callister, S.J., Nicora, C.D., Zeng, X., Roh, J.H., Dominguez, M.A., Tavano, C.L., Monroe, M.E., Kaplan, S., Donohue, T.J., Smith, R.D., et al. (2006). Comparison of aerobic and photosynthetic *Rhodobacter sphaeroides* 2.4.1 proteomes. J. Microbiol. Methods *67*, 424–436. https://doi.org/10.1016/j.mimet.2006.04.021.

57. Selao, T.T., Branca, R., Chae, P.S., Lehtiö, J., Gellman, S.H., Rasmussen, S.G.F., Nordlund, S., and Norén, A. (2011). Identification of chromatophore membrane protein complexes formed under different nitrogen availability conditions in *Rhodospirillum rubrum*. J. Proteome Res. *10*, 2703–2714. https://doi.org/10.1021/pr100838x.

58. Fejes, A.P., Yi, E.C., Goodlett, D.R., and Beatty, J.T. (2003). Shotgun proteomic analysis of a chromatophore-enriched preparation from the purple phototrophic bacterium *Rhodopseudomonas palustris*. Photosynth. Res. *78*, 195–203. https://doi.org/10.1023/B:PRES.0000006752.81486.74.

59. Lohsse, A., Ullrich, S., Katzmann, E., Borg, S., Wanner, G., Richter, M., Voigt, B., Schweder, T., and Schüler, D. (2011). Functional analysis of the magnetosome island in *Magnetospirillum gryphiswaldense*: the mamAB operon is sufficient for magnetite biomineralization. PLoS One *6*, e25561. https://doi.org/10.1371/journal.pone.0025561.

60. Lohße, A., Borg, S., Raschdorf, O., Kolinko, I., Tompa, E., Pósfai, M., Faivre, D., Baumgartner, J., and Schüler, D. (2014). Genetic dissection of the mamAB and mms6 operons reveals a gene set essential for magnetosome biogenesis in *Magnetospirillum gryphiswaldense*. J. Bacteriol. *196*, 2658–2669. https://doi.org/10.1128/JB.01716-14.

61. Tang, J., Zhang, K., Dong, J., Yan, C., Hu, C., Ji, H., Chen, L., Chen, S., Zhao, H., and Song, Z. (2020). Sam50-Mic19-Mic60 axis determines mitochondrial cristae architecture by mediating mitochondrial outer and inner membrane contact. Cell Death Differ. *27*, 146–160. https://doi.org/10.1038/s41418-019-0345-2.

62. van der Laan, M., Bohnert, M., Wiedemann, N., and Pfanner, N. (2012). Role of MINOS in mitochondrial membrane architecture and biogenesis. Trends Cell Biol. *22*, 185–192. https://doi.org/10.1016/j.tcb.2012.01.004.

63. Ott, C., Dorsch, E., Fraunholz, M., Straub, S., and Kozjak-Pavlovic, V. (2015). Detailed analysis of the human mitochondrial contact site complex indicate a hierarchy of subunits. PLoS One *10*, e0120213. https://doi.org/10.1371/journal.pone.0120213.

64. Anwari, K., Poggio, S., Perry, A., Gatsos, X., Ramarathinam, S.H., Williamson, N.A., Noinaj, N., Buchanan, S., Gabriel, K., Purcell, A.W., et al. (2010). A modular BAM complex in the outer membrane of the α-proteobacterium Caulobacter crescentus. PLoS One *5*, e8619. https://doi.org/10.1371/journal.pone.0008619.

65. Anwari, K., Webb, C.T., Poggio, S., Perry, A.J., Belousoff, M., Celik, N., Ramm, G., Lovering, A., Sockett, R.E., Smit, J., et al. (2012). The evolution of new lipoprotein subunits of the bacterial outer membrane BAM complex. Mol. Microbiol. *84*, 832–844. https://doi.org/10.1111/j.1365-2958.2012.08059.x.

66. Jiao, Y., Kappler, A., Croal, L.R., and Newman, D.K. (2005). Isolation and characterization of a genetically tractable photoautotrophic Fe(II)-oxidizing bacterium, *Rhodopseudomonas palustris* strain TIE-1. Appl.

Environ. Microbiol. *71*, 4487–4496. https://doi.org/10.1128/AEM.71.8.4487-4496.2005.

67. Brimacombe, C.A., Stevens, A., Jun, D., Mercer, R., Lang, A.S., and Beatty, J.T. (2013). Quorum-sensing regulation of a capsular polysaccharide receptor for the *Rhodobacter capsulatus* gene transfer agent (RcGTA). Mol. Microbiol. *87*, 802–817. https://doi.org/10.1111/mmi.12132.
68. Quandt, J., and Hynes, M.F. (1993). Versatile suicide vectors which allow direct selection for gene replacement in Gram-negative bacteria. Gene *127*, 15–21. https://doi.org/10.1016/0378-1119(93)90611-6.
69. Ind, A.C., Porter, S.L., Brown, M.T., Byles, E.D., de Beyer, J.A., Godfrey, S.A., and Armitage, J.P. (2009). Inducible-expression plasmid for *Rhodobacter sphaeroides* and *Paracoccus denitrificans*. Appl. Environ. Microbiol. *75*, 6613–6615. https://doi.org/10.1128/AEM.01587-09.
70. Khan, S.R., Gaines, J., Roop, R.M., and Farrand, S.K. (2008). Broad-host-range expression vectors with tightly regulated promoters and their use to examine the influence of TraR and TraM expression on Ti plasmid quorum sensing. Appl. Environ. Microbiol. *74*, 5053–5062. https://doi.org/10.1128/AEM.01098-08.
71. Lee, M.D. (2019). GToTree: a user-friendly workflow for phylogenomics. Bioinformatics *35*, 4162–4164. https://doi.org/10.1093/bioinformatics/btz188.
72. Nguyen, L.T., Schmidt, H.A., von Haeseler, A., and Minh, B.Q. (2015). IQ-TREE: a fast and effective stochastic algorithm for estimating maximum-likelihood phylogenies. Mol. Biol. Evol. *32*, 268–274. https://doi.org/10.1093/molbev/msu300.
73. Parks, D.H., Chuvochina, M., Rinke, C., Mussig, A.J., Chaumeil, P.A., and Hugenholtz, P. (2022). GTDB: an ongoing census of bacterial and archaeal diversity through a phylogenetically consistent, rank normalized and complete genome-based taxonomy. Nucleic Acids Res. *50*, D785–D794. https://doi.org/10.1093/nar/gkab776.
74. Mai, U., and Mirarab, S. (2018). TreeShrink: fast and accurate detection of outlier long branches in collections of phylogenetic trees. BMC Genomics *19*, 272. https://doi.org/10.1186/s12864-018-4620-2.
75. Menardo, F., Loiseau, C., Brites, D., Coscolla, M., Gygli, S.M., Rutaihwa, L.K., Trauner, A., Beisel, C., Borrell, S., and Gagneux, S. (2018). Treemmer: a tool to reduce large phylogenetic datasets with minimal loss of diversity. BMC Bioinformatics *19*, 164. https://doi.org/10.1186/s12859-018-2164-8.
76. Ehrenreich, A., and Widdel, F. (1994). Anaerobic oxidation of ferrous iron by purple bacteria, a new type of phototrophic metabolism. Appl. Environ. Microbiol. *60*, 4517–4526.
77. Jun, D., Saer, R.G., Madden, J.D., and Beatty, J.T. (2014). Use of new strains of *Rhodobacter sphaeroides* and a modified simple culture medium to increase yield and facilitate purification of the reaction centre. Photosynth. Res. *120*, 197–205. https://doi.org/10.1007/s11120-013-9866-6.
78. Beatty, J.T., and Gest, H. (1981). Biosynthetic and bioenergetic functions of citric acid cycle reactions in *Rhodopseudomonas capsulata*. J. Bacteriol. *148*, 584–593. https://doi.org/10.1128/jb.148.2.584-593.1981.
79. Mistry, J., Chuguransky, S., Williams, L., Qureshi, M., Salazar, G.A., Sonnhammer, E.L.L., Tosatto, S.C.E., Paladin, L., Raj, S., Richardson, L.J., et al. (2021). Pfam: the protein families database in 2021. Nucleic Acids Res. *49*, D412–D419. https://doi.org/10.1093/nar/gkaa913.
80. Zhou, Z., Tran, P.Q., Breister, A.M., Liu, Y., Kieft, K., Cowley, E.S., Karaoz, U., and Anantharaman, K. (2022). METABOLIC: high-throughput profiling of microbial genomes for functional traits, metabolism, biogeochemistry, and community-scale functional networks. Microbiome *10*, 33. https://doi.org/10.1186/s40168-021-01213-8.
81. Baba, T., Ara, T., Hasegawa, M., Takai, Y., Okumura, Y., Baba, M., Datsenko, K.A., Tomita, M., Wanner, B.L., and Mori, H. (2006). Construction of *Escherichia coli* K-12 in-frame, single-gene knockout mutants: the Keio collection. Mol. Syst. Biol. *2*, 2006.0008. https://doi.org/10.1038/msb4100050.
82. Welander, P.V., Doughty, D.M., Wu, C.H., Mehay, S., Summons, R.E., and Newman, D.K. (2012). Identification and characterization of *Rhodopseudomonas palustris* TIE-1 hopanoid biosynthesis mutants. Geobiology *10*, 163–177. https://doi.org/10.1111/j.1472-4669.2011.00314.x.
83. Pinto, F.L., Thapper, A., Sontheim, W., and Lindblad, P. (2009). Analysis of current and alternative phenol based RNA extraction methodologies for cyanobacteria. BMC Mol. Biol. *10*, 79. https://doi.org/10.1186/1471-2199-10-79.
84. Pfaffl, M.W. (2001). A new mathematical model for relative quantification in real-time RT-PCR. Nucleic Acids Res. *29*, e45. https://doi.org/10.1093/nar/29.9.e45.
85. Schneider, C.A., Rasband, W.S., and Eliceiri, K.W. (2012). NIH Image to ImageJ: 25 years of image analysis. Nat. Methods *9*, 671–675. https://doi.org/10.1038/nmeth.2089.
86. Mastronarde, D.N. (2005). Automated electron microscope tomography using robust prediction of specimen movements. J. Struct. Biol. *152*, 36–51. https://doi.org/10.1016/j.jsb.2005.07.007.
87. Mastronarde, D.N., and Held, S.R. (2017). Automated tilt series alignment and tomographic reconstruction in IMOD. J. Struct. Biol. *197*, 102–113. https://doi.org/10.1016/j.jsb.2016.07.011.
88. Cohen-Bazire, G., Sistrom, W.R., and Stanier, R.Y. (1957). Kinetic studies of pigment synthesis by non-sulfur purple bacteria. J. Cell. Comp. Physiol. *49*, 25–68. https://doi.org/10.1002/jcp.1030490104.
89. Cox, J., Hein, M.Y., Luber, C.A., Paron, I., Nagaraj, N., and Mann, M. (2014). Accurate proteome-wide label-free quantification by delayed normalization and maximal peptide ratio extraction, termed MaxLFQ. Mol. Cell. Proteomics *13*, 2513–2526. https://doi.org/10.1074/mcp.M113.031591.

Please cite this article in press as: Muñoz-Gómez et al., Intracytoplasmic-membrane development in alphaproteobacteria involves the homolog of the mitochondrial crista-developing protein Mic60, Current Biology (2023), https://doi.org/10.1016/j.cub.2023.02.059

STAR★METHODS

KEY RESOURCES TABLE

REAGENT or RESOURCE	SOURCE	IDENTIFIER
Antibodies		
6x-His Tag Monoclonal Antibody (HIS.H8)	Thermo Fisher Scientific	Catalog#: MA1-21315; RRID: AB_557403
HRP-conjugated Anti-Mouse Antibody	Bio-Rad	Cat# 1706516; RRID: AB_11125547
Bacterial strains		
Escherichia coli TOP10	Thermo Fisher Scientific	Catalog#: C404003
Escherichia coli S17-1- λpir-RP4	J. Thomas Beatty (University of British Columbia)	S17-1 λ*pir*
Escherichia coli DH5α	Thermo Fisher Scientific	Catalog#: 18258012
Escherichia coli DH5α-λpir	J. Thomas Beatty (University of British Columbia)	DH5α λpir
Escherichia coli BW29427-λpir-RP4	J. Thomas Beatty (UBC). Originally isolated by W. R. Sistrom (University of Oregon)	BW29427 λpir
Chemicals, peptides, and recombinant proteins		
Proteinase K, recombinant, PCR Grade	Sigma Aldrich (Roche)	Catalog#: 000000003115879001
Digitonin	Sigma Aldrich	Catalog#: D141
Triton X-100	Thermo Fisher Scientific	Catalog#: HFH10
Dynabeads His-Tag Isolation and Pulldown	Thermo Fisher Scientific	Catalog#: 10104D
Coomassie Brilliant Blue G-250	Thermo Fisher Scientific	Catalog#: 20279
DNAse I	Qiagen	Catalog#: 79254
Dimethyl pimelimidate dihydrochloride	Sigma Aldrich	Catalog#: D8388
Critical commercial assays		
ZR Bacterial DNA Miniprep Kit	Zymo Research	Catalog#: D6005
Epicentre MasterPure DNA and RNA Purification Kit	Epicentre Biotechnologies	Catalog#: MC85200
Gibson Assembly Master Mix	New England Biolabs	Catalog#: E2611L
AxyPrep Plasmid Miniprep Kit	Axygen	Catalog#: AP-MN-P-250
NEB Builder HiFi DNA Assembly	New England Biolabs	Catalog#: E5520S
Gibson Assembly Cloning Kit	New England Biolabs	Catalog#: E5510S
Strand cDNA Synthesis Kit	Roche	Catalog#: 11483188001
Bolt 4-12% Bis-Tris Plus Gel	Invitrogen	Catalog#: NW04120BOX
NativePAGE Sample Buffer	Invitrogen	Catalog#: 10655853
3-12% Bis-Tris BNE Gel	Invitrogen	Catalog#: BN1003BOX
Deposited data		
Rhodobacter sphaeroides Mic60-6X-His immunoprecipitation	PRIDE	ID#: PXD032747
Rhodobacter sphaeroides Orf52-6X-His immunoprecipitation	PRIDE	ID#: PXD032747
Experimental models: Cell lines		
Rhodobacter sphaeroides Δ*mic60*	This study	N/A
Rhodobacter sphaeroides Δ*orf52*	This study	N/A
Rhodobacter sphaeroides mic60↑	This study	N/A
Rhodobacter sphaeroides orf52↑	This study	N/A
Rhodobacter sphaeroides mic60-6X-His	This study	N/A
Rhodobacter sphaeroides orf52-6X-His	This study	N/A

(*Continued on next page*)

Please cite this article in press as: Muñoz-Gómez et al., Intracytoplasmic-membrane development in alphaproteobacteria involves the homolog of the mitochondrial crista-developing protein Mic60, Current Biology (2023), https://doi.org/10.1016/j.cub.2023.02.059

Continued

REAGENT or RESOURCE	SOURCE	IDENTIFIER
Rhodopseudomonas palustris Δ*mic60*	This study	N/A
Rhodopseudomonas palustris Δ*orf52*	This study	N/A
Rhodopseudomonas palustris mic60↑	This study	N/A
Rhodopseudomonas palustris orf52↑	This study	N/A
Rhodopseudomonas palustris mic60-6X-His	This study	N/A
Rhodopseudomonas palustris orf52-6X-His	This study	N/A
Experimental models: Organisms/strains		
Rhodobacter sphaeroides	J. Thomas Beatty (UBC). Originally isolated by W. R. Sistrom (University of Oregon)	2.4.1
Rhodopseudomonas palustris	Jiao et al.[66]	TIE-1
Oligonucleotides		
For oligonucleotides used in this study, see Table S1	N/A	N/A
Recombinant DNA		
pZDJ	Brimacombe et al.[67]	N/A
pZDJ-ΔRSP6207	This study	N/A
pZDJ-ΔRSP1508	This study	N/A
PJQ200SK	Quandt and Hynes[68]	N/A
PJQ200SK-ΔRS01285	This study	N/A
PJQ200SK-ΔRS01290	This study	N/A
pIND4-Km	Ind et al.[69]	N/A
pIND4-Km-RSP_6207-6xHis	This study	N/A
pIND4-Gm	Alexander Westbye (University of British Columbia)	N/A
pIND4-Gm-RSP_1508-6xHis	This study	N/A
pSRK-Km	Khan et al.[70]	N/A
pSRK-Km-RS01285-6xHis	This study	N/A
pSRK-Gm	Khan et al.[70]	N/A
pSRK-Gm-RS01290-6xHis	This study	N/A
Software and algorithms		
GraphPad Prism 7	GraphPad	https://www.graphpad.com/
Image Lab	Bio-Rad	http://www.bio-rad.com/en-de/product/image-lab-software?ID=KRE6P5E8Z
CFX Maestro software	Bio-Rad	https://www.bio-rad.com/en-cz/product/cfx-maestro-software-for-cfx-real-time-pcr-instruments?ID=OKZP7E15
GToTree	Lee[71]	https://github.com/AstrobioMike/GToTree/wiki/installation
IQ-TREE	Nguyen et al.[72]	http://www.iqtree.org/
GTDB R207	Parks et al.[73]	https://gtdb.ecogenomic.org/stats/r207
TreeShrink	Mai and Mirarab[74]	https://uym2.github.io/TreeShrink/
Treemmer	Menardo et al.[75]	https://github.com/fmenardo/Treemmer
opm R package	N/A	https://github.com/mdphan/GrowthCurvesAnalysis_shinyApp

RESOURCE AVAILABILITY

Lead contact

Further information and requests for resources and reagents should be directed to and will be fulfilled by the lead contact, Sergio A. Muñoz-Gómez (samunozg@purdue.edu).

Please cite this article in press as: Muñoz-Gómez et al., Intracytoplasmic-membrane development in alphaproteobacteria involves the homolog of the mitochondrial crista-developing protein Mic60, Current Biology (2023), https://doi.org/10.1016/j.cub.2023.02.059

Materials availability

- Plasmids generated in this paper is available from the lead contact upon request.
- Bacterial strains generated in this paper is available from the lead contact upon request.
- This study did not generate new unique reagents.

Data and code availability

- LC-MS/MS data have been deposited at ProteomeXchange Consortium (http://www.proteomexchange.org) and are publicly available as of the date of publication. Accession numbers are listed in the key resources table.
- This paper does not report original code.
- Any additional information required to reanalyze the data reported in this paper is available from the lead contact upon request.

EXPERIMENTAL MODEL AND SUBJECT DETAILS

Bacterial strains, media, and growth conditions

R. palustris TIE-1 and *E. coli* BW29427-λpir-RP4 were kindly provided by Dianne K. Newman (California Institute of Technology).[66] *R. sphaeroides* 2.4.1, *E. coli* S17-1- λpir, and *E. coli* DH5α-λpir were kindly provided by Jeanette Johnson-Beatty (University of British Columbia). *R. palustris* TIE-1 strain was grown both chemo- and photoheterotrophically at 30 °C in YPS rich medium,[66] unless otherwise noted. *R. palustris* TIE-1 was grown photoheterotrophically at 30 °C on FEM minimal medium.[76] *R. sphaeroides* 2.4.1 strain was grown chemoheterotrophically at 30 °C in LB or RLB rich media,[77] unless otherwise noted, and photoheterotrophically at 30 °C on RCVBN minimal medium.[78]

For growth analysis under photoheterotrophic conditions, *R. sphaeroides* and *R. palustris* WT and mutant strains were grown in front to three incandescent 40 W lightbulbs at a temperature of 29 °C, with the distances of the culture tubes from the light sources adjusted to allow the appropriate light intensities and temperature. The light intensities were measured to be ∼200 μmol photons m^{-2} s^{-1} for high light and ∼10 μmol photons m^{-2} s^{-1} for low light. The latter was achieved by placing the two layers of approximately ∼50 % neutral density filter sheeting between the light source and culture tubes. Prior to growth analysis, cells were grown in in rich media in triplicate (*R. sphaeroides*, RLB without antibiotics; *R. palustris*, YPS no antibiotic for WT, 400 μg/ml kanamycin for mutants) until mid-log phase. At mid-log phase equivalent amounts of cells (turbidity x volume = 20, i.e., if the turbidity value was equal to 5.10, then 3.92 ml of cells were decanted) were removed from the growth tubes into 15 ml Falcon tubes and pelleted by centrifugation. The pellet was washed once in minimal media and resuspended in 1 ml of the required minimal media (*R. sphaeroides* 10 ml RCVBN + 8 ml RLB and *R. palustris* FEM). A 150 μl volume was of each cell line suspension was inoculated in triplicate; this was time point 0. Turbidity measurements were performed using a McFarland Densitometer DEN-1B that measures at λ = 565 ±15 nm. Turbidity measurements were then taken every 6 h for a total experiment length of 72 h. For analysis of chemoheterotrophic growth, the same approach was made except the cell cultures were grown in the dark in well-aerated flasks that were under constant agitation to ensure gas exchange. Whole-cell absorption spectra of these cells were measured to verify the absence of RC-LH1 and LH2 complexes under these conditions (Figure S3D). Growth parameters were analysed using the opm R package (https://github.com/mdphan/GrowthCurvesAnalysis_shinyApp). Spectra were recorded from bacterial strains grown to late-log phase at all photoheterotrophic and chemoheterotrophic conditions after resuspension in MES buffer pH 6.8 resuspended to OD ∼6,5. The absorption spectra were measured at 0.5 nm intervals using a Shimadzu UV-Vis-NIR UV2600 spectrophotometer equipped with an integrating sphere. The resulting spectra were normalised to OD = 1 at the BChl Qx (∼ 590 nm) peak for comparison.

METHOD DETAILS

Bioinformatic analysis

To survey the genetic context of *mic60*, homologs were identified through similarity searches and a neighboring region of ±6 Kbp was extracted from each selected alphaproteobacterial genome. The identification of up- and downstream genes was done visually by relying on genome annotations. To build a reference phylogenetic tree, a supermatrix of 117 single-copy marker genes for the selected alphaproteobacterial genomes was assembled with GToTree.[71] The compositional heterogeneity of the supermatrix was then decreased with ζtrimmer, and a phylogenetic tree was finally inferred with IQ-TREE and the LG+C60+F+G4 model.[72]

To generate the comprehensive phylogenetic tree that summarizes the phylogenetic and physiological diversity in the *Alphaproteobacteria* (Figure 1B), a maximally diverse set of 705 taxa was down sampled from >7,684 genomes in the GTDB R207 database.[73] The down sampling was performed with Treemmer[75] and constrained in such a way that all taxa with ICMs and ICM-associated physiologies were retained. A supermatrix of single-copy marker genes was assembled with GTDB-Tk, a phylogenetic tree was inferred with IQ-TREE (-fast mode), and the longest-branching taxa were subsequently identified and removed with TreeShrink.[74] Similarity searches of ICM-associated marker proteins (NxrAXBCD, PmoABC, PufLM, RbcI, RbcII; see Figure 1B) were performed with the program hmmsearch of the HMMER suite using both Pfam and custom pHMMs[79] derived from the METABOLIC software.[80] TreeViewer was used to display the phylogenetic distributions of traits on the tree.

DNA methods and plasmid construction

Total genomic DNA (gDNA) was extracted from *R. sphaeroides* and *R. palustris* strains using the ZR Bacterial DNA Miniprep Kit (Zymo Research) with a BIO101/Savant FastPrep FP120 high-speed bead beater and a 30 min incubation at 60°C with 20 μl of proteinase K (20 mg/mL), or the Epicentre MasterPure DNA Purification Kit (Epicentre Biotechnologies). All plasmid constructs were built with the Gibson Assembly Master Mix or the NEB Builder HiFi DNA Assembly (both New England Biolabs). Plasmids were isolated using the AxyPrep Plasmid Miniprep Kit (Axygen). All plasmid constructs were confirmed by Sanger sequencing using both forward and reverse primers. Table S1 lists all primers used in this study.

Construction of *R. sphaeroides* and *R. palustris* knockout strains

To knockout genes in *R. sphaeroides*, a knockout construct was assembled into the suicide plasmid vector pZDJ[67] with either the Gibson Assembly Cloning Kit or the NEBuilder HiFi DNA Assembly Master Mix (both New England Biolabs). The antibiotic resistance cassette flanked by flippase recognition target (FRT) sites used to knocked out the genes corresponds to that used in the Keio collection.[81] The resulting suicide vector with the knockout construct was cloned into *E. coli* S17-1 λ-pir-RP4, which can replicate the suicide plasmid. This strain was then conjugated with *R. sphaeroides 2.4.1*. Briefly, donor and recipient cells grown to stationary phase were mixed in a 1:2 volume ratio and pelleted by centrifugation for 1 min at 4,500-6,000 × g, and then washed twice with antibiotic-free RCVBN minimal medium. After the last wash, the pellet was resuspended in 50 μl of RCVBN, and 10 μl aliquots were spotted onto antibiotic-free RCVBN solid medium. The plates were incubated at 30° C overnight to allow conjugation to take place. Afterwards, an emulsion was made from the several inoculation spots and streaked onto antibiotic-containing RCVBN+Gm solid medium. *R. sphaeroides* exconjugants were then successively streaked onto new LB+Gm solid medium until no *E. coli* S17-1 λ-pir-RP4 contamination remained. The resulting pure *R. sphaeroides* exconjugants contained the pZDJ plasmid, with the knockout gene construct, integrated in the chromosome by a first crossing over (recombination) event. To induce a second crossing over to excise the pZDJ suicide plasmid from the host chromosome, colonies were picked and grown on liquid LB with no antibiotic selection until late stationary phase (about 2-3 days). The cultures were then streaked on LB+10% sucrose solid medium, which allows for counter-selection of those colonies that have lost the integrated pZDJ plasmid. The counter-selection relies on the *sacB* gene carried by the suicide plasmid.[43] In order to induce a third crossing over between the FRT sites of the kanamycin cassette, cells were grown in liquid LB without any antibiotic selection until late stationary phase and then streaked on LB solid medium. Resultant colonies were then screened through PCR assays.

To make knockout strains for *R. palustris*, the same general protocol used for *R. sphaeroides* was followed.[82] The suicide plasmid used for *R. palustris* was pJQ200SK[68] and the host strain was *E. coli* BW29427-λpir-RP4, which requires 300 μM diaminopimelic acid for growth. This auxotrophy allows to easily remove the plasmid-donor bacterium from the medium after conjugation.

Construction of *R. sphaeroides* and *R. palustris* overexpression strains

To create Mic60- and Orf52-overexpressing strains, the inducible expression plasmids for *R. sphaeroides* pIND4 -Km and pIND4-Gm were kindly provided by Judith P. Armitage (University of Oxford), and Alexander Westbye (University of British Columbia), respectively. The inducible expression plasmid pSRK was used for *R. palustris*. The coding sequences of the *mic60* and *orf52* genes of *R. sphaeroides* and *R. palustris* were amplified by PCR and assembled into the expression vectors pIND4 and pSRK, respectively, with the NEBuilder HiFi DNA Assembly Master Mix (New England Biolabs). The *mic60* and *orf52* homologs were cloned into kanamycin resistance-conferring plasmids and gentamycin resistance-conferring plasmids, respectively. To insert the C-terminal 6xHis tag as part of the coding sequences of *mic60* and *orf52*, the BamHI and BglII restriction sites in pIND4 were used, or the tag was incorporated as part of the primer used to amplify the targets in *R. palustris*. Conjugative *E. coli* hosts were transformed by the assembled plasmids, and conjugation assays with recipient *R. sphaeroides* and *R. palustris* strains were done as described above. After conjugation, the exconjugants were repeatedly streaked onto antibiotic-containing plates to remove the plasmid-donor bacterium. The resulting overexpression strains were further verified by RT qPCR.

RT qPCR

R. sphaeroides and *R. palustris* strains were grown in triplicate until mid-log phase as described for growth analysis, after which 1 mM IPTG was added, and the cells allowed to grow for 7 h 20 min for *R. sphaeroides* and 4 h 30 min for *R. palustris*; cultures were grown in parallel in the absence of IPTG. Then 1 ml of cell suspension was centrifuged and the pellet resuspended in 1 ml of PGTX nucleic acid extraction buffer.[83] The samples were then flash frozen and stored at -20 °C until the PGTX-mediated nucleic acid extraction procedure, essentially following the classical phenol/chloroform extraction method.[83] Briefly, isolated total nucleic acid concentration was measured using a NanoDrop DeNovix DS-11 (Thermo Fisher) and diluted to 100 ng/μL in 50 μl DNase/RNase-free H_2O. The digestion of gDNA was performed by addition of DNase I (Qiagen) and the concentration of total RNA was measured using the Qubit 2.0 Fluorometer (Thermo Fisher). A total of 100 ng RNA was subsequently reverse transcribed using the Transcriptor First Strand cDNASynthesis Kit (Roche) at 55 °C for cDNA synthesis. Quantitative PCR (qPCR) was performed in triplicates in a CFX96 qPCR cycler (Bio-Rad) in 20 μl reactions containing 1x PowerUp SYBR Green master mix (Applied Biosystems, USA), 8 pmol of each primer, and 10 μg cDNA with the following program: initial denaturation 10 min at 95 °C; 45 cycles of 15 s at 95 °C and 30 s at 60 °C. Primers annealing to *mic60*, *orf52*, and the *rpoZ* cDNAs used for qPCR are listed in Table S1. Cycle threshold values were automatically computed with the CFX Maestro software (Bio-Rad). Additionally, non-reverse transcribed RNA sample was used as a control to verify complete degradation of genomic DNA. Relative abundance of transcripts in cells grown in the presence of IPTG

compared to those grown without the inducing agent was calculated using the $2^{-\Delta\Delta CT}$ method[84]; the unaffected *rpoZ* housekeeping gene cDNA was used to normalize the *mic60* and *orf52* values.

Transmission electron microscopy

Both classical TEM and electron tomography on cryopreserved samples cut into 80 nm-thick sections were done as previously described.[17,53] Cells were centrifuged at 620 x g for 10 min at RT and the cell pellet was mixed with a drop of 20% BSA and transferred into gold-plated specimen carriers (thickness 0,5mm, thick diameter 1.2 mm, depth 200 μm; Leica). The carriers were immediately applied a Leica EM Pact2 high pressure freezing (HPF). Freeze substitution was then performed in 2% OsO4 diluted in 100% acetone at -90C for 96 h. Samples were subsequently warmed to -20C at a rate 5C/h. After 24 h, the temperature was increased to 4C at a rate of 3C/h. After freeze substitution, cells were rinsed 3 times for 15 min in 100% acetone at RT. Then they were infiltrated in 25%, 50%, 75% Spurr resin solutions for 1 h at each step. After overnight 100C incubation, the samples were polymerized in 100% Spurr resin at 62C for 48 h. Ultrathin sections were then counterstained with ethanolic uranyl acetate (30 min) and lead citrate (20 min). For electron tomography, both sides of sections were covered by gold nanoparticles of 10 nm in diameter (BBI) and carbon coated.

Scoring of *R. palustris* ICM area/TEM area and *R. sphaeroides* tubules/cell per section were performed blinded on images obtained using JEOL 1010 TEM operating at an accelerating voltage of 80 kV and equipped with a MegaView III CCD camera (SIS). Measurement of *R. palustris* ICM and total cell areas was done using Image J software[85] by tracing along the outermost electron dense membranes of the ICM network and the outer membrane, respectively. The occurrence of tubule-like and branching ICMs in *R. sphaeroides* was counted on 20-21 images that were taken at 40,000x magnification (2.56 nm/pixel) at random parts of the grid as before.[17] These images were mixed and randomized prior to blind scoring.

Electron tomograms were collected at a range of ±65° with tilt 1° steps using the JEOL 2100F TEM working at 200 kV, equipped with Gatan camera K2 Summit and controlled with SerialEM automated acquisition software.[86] IMOD software[87] was used for tomogram reconstruction and generating 3D models by segmentation.

SDS PAGE and Western blotting

Bacterial lysates were separated on a Bolt 4-12% Bis-Tris Plus gel (Invitrogen), blotted onto a PVDF membrane (Amersham), blocked in 5% low-fat, powdered milk (w/v) in phosphate buffered saline with 0.1% Tween 20 (v/v) (PBS-T), and probed with 6x-His Tag Monoclonal Antibody (HIS.H8) (Thermo Fisher Scientific #MA1-21315) diluted in 5% milk in PBS-T (1:500). This was followed by incubation with secondary HRP-conjugated anti-mouse antibody (1:2000; Bio-Rad). Proteins were visualized using the Pierce ECL system (Genetica/Bio-Rad) on a ChemiDoc imager (Bio-Rad).

Isolation of ICMs via high-pressure homogenization and light spectroscopy

R. sphaeroides strains were cultured identically in C-succinate media[88] in flat, glass bottles at 28-30°C under anaerobic conditions. Illumination was provided by one incandescent 40W bulb providing ~10 μmol photons m^{-2} s^{-1}. The cells were fully adapted to the incident light-intensity and harvested by centrifugation once they had reached mid-log phase. Cell pellets were washed in 20 mM MES, 100 mM KCl, pH 6.8, then flash frozen and stored at −80 °C until required

The cell pellets were re-suspended in 20 mM Tris.Cl, pH 8.0 and homogenised thoroughly with a few grains of DNAse I (Qiagen) and a few mg of $MgCl_2$. The cells were broken by passage three times through an Emulsiflex-C5 cell disrupter (Avestin). The ruptured cell solution was first subjected to a low-speed centrifugation step (10 min, 10,000 × *g*, 4°C) to remove any unbroken cells. The decanted supernatant was ultra-centrifuged (120 min, 180,000 × *g*, 4°C), after which the supernatant was discarded. The resulting chromatophore pellet was gently re-suspended in 20 mM Tris-HCl pH 8.0 before the optical density was adjusted to 10 cm^{-1} at the Qx absorption maximum (~590 nm) using a Shimadzu UV-Vis-NIR UV2600 spectrophotometer equipped with an integrating sphere.

Blue Native PAGE

BN-PAGE of isolated ICMs was adapted from published protocols.[53] Briefly, 1 mg of total protein was resuspended in 100 μl NativePAGE sample buffer (Invitrogen), lysed with 1.5% digitonin (v/v) and 0.1% Triton X-100 (v/v) for 1 h on ice then cleared by centrifugation (22,000 × g, 20 min, 4 °C). Subsequently, 5% Coomassie brilliant blue G-250 was added before loading ~100 μg on a 3-12% Bis-Tris BNE gel (Invitrogen). After electrophoresis (2.5 hours, 150 V, 4 °C), the gel was blotted onto a PVDF membrane (Amersham) and probed as described above.

Affinity purification

Affinity purification (AP) of tagged proteins from 1 mg isolated ICMs were solubilized in IPP50 buffer (50 mM KCl, 20 mM Tris-HCl pH 7.7, 3 mM $MgCl_2$, 10% glycerol, 1 mM phenylmethanesulfonyl fluoride, complete EDTA free protease inhibitor cocktail (Roche) supplemented with 1.5% digitonin (v/v) and 0.1% Triton X-100 (v/v)) for 1 h on ice. After centrifugation (22,000 ×g, 20 min, 4 °C) the supernatant was added to 2.0 mg of cobalt conjugated Dynabeads (Thermo Fisher) to capture the His-tag. The Dynabeads were pre-washed in 300 μl of IPP50 + 1.5% digitonin for 5 min at RT. The solubilized ICMs were rotated with beads for 90 min at 4 °C. After removal of the flow-through, the beads were washed three times in IPP50 + 1.5% digitonin. Prior to eluting, the beads were transferred into a new tube. Elution was done with 300 mM imidazole in IPP50 for 15 min at RT and shaking at 1000 rpm. The elutes were further processed for LC-MS^2 analysis or resolved by SDS-PAGE. APs were performed in triplicate.

Protein preparation and mass spectroscopy

Individual bands containing proteins of interest were excised from Coomassie stained SDS PAGE gel using a razor blade and cut into small pieces (~1 mm^3). Bands were destained by sonication for 30 min in 50% acetonitrile (ACN) and 50 mM ammonium bicarbonate (ABC). After destaining, gels were dried in ACN. Disulfide bonds were reduced using 10mm DTT in 100mM ABC at 60°C for 30 min. After that, samples were again dried with ACN and free cysteine residues were blocked using 55 mM iodoacetamide in 100 mM ABC for 10 min at room temperature in the dark. Samples were dried thoroughly and then digestion buffer (10% ACN, 40 mM ABC and 13 ng/μl trypsin) was added to cover gel pieces. Proteins were digested at 37 °C overnight. After digestion, 150 μl of 50% ACN with 0.5% formic acid was added and sonicated for 30 min. Supernatant containing peptides was transferred to a new microcentrifuge tube and another 150 μl of elution solution was added and sonicated for 30 min. This solution was removed, combined with the previous solution and dried by SpeedVac. Dried peptides were reconstitued in 2% ACN with 0.1% TFA and injected into Ultimate 3000 Nano LC coupled to Orbitrap Fusion.

Eluates of co-AP proteins and thin-sliced BN-PAGE gels were processed for MS analysis as described elsewhere.[53] In brief, eluate samples were resuspended in 100 mM tetraethylammonium bromide containing 2% sodium deoxycholate. Cysteines were reduced with 10 mM tris(2-carboxyethyl)phosphine and subsequently cleaved with 1 μg trypsin overnight at 37 °C. After digestion, 1% trifluoroacetic acid (TFA) was added to wash twice and eluates were resuspended in 20 μl TFA per μg of protein. A nano reversed-phased column (EASY-Spray column, 50 cm x 75 μm inner diameter, PepMap C18, 2 μm particles, 100 Å pore size) was used for LC/MS analysis. Mobile phase buffer A consisted of water and 0.1% formic acid. Mobile phase D consisted of acetonitrile and 0.1% formic acid. Samples were loaded onto the trap column (Acclaim PepMap300, C18, 5 μm, 300 Å pore size, 300 μm x 5 mm) at a flow rate of 15 μl/min. The loading buffer consisted of water, 2% acetonitrile, and 0.1% TFA. Peptides were eluted using a Mobile phase B gradient from 2% to 40% over 60 min at a flow rate of 300 ml/min. The peptide cations eluted were converted to gas-phase ions via electrospray ionization and analyzed on a Thermo Orbitrap Fusion (Q-OT- qIT, Thermo Fisher). Full MS spectra were acquired in the Orbitrap with a mass range of 350-1, 400 *m/z*, at a resolution of 120,000 at 200 *m/z* and with a maximum injection time of 50 ms. Tandem MS was performed by isolation at 1.5 Th with the quadrupole, high-energy collisional dissociation (HCS) fragmentation with normalized collision energy of 30, and rapid scan MS analysis in the ion trap. The MS/MS ion count target was set to 10^4 and the max infection time at 35 ms. Only those precursors with a charge state of 2-6 were sampled. The dynamic exclusion duration was set to 45 s with a 10 ppm tolerance around the selected precursor and its isotopes. Monoisotopic precursor selection was on with a top speed mode of 2 s cycles.

Analysis of mass spectroscopy peptides

Label-free quantification of the data were analyzed using the MaxQuant software (version 1.6.2.1).[89] The false discovery rates for peptides and for proteins was set to 1% with a specified minimum peptide length of seven amino acids. The Andromeda search engine was used for the MS/MS spectra against the *R. sphaeroides* 2.4.1 predicted proteome (ASM1290v2) downloaded from NCBI GenBank on October 2020. Enzyme specificity was set to C-terminal Arg and Lys, alongside for cleavage at proline bonds with a maximum of two missed cleavages. Dithiomethylation of cysteine was selected as a fixed modification with N-terminal protein acetylation and methionine oxidation as variable modifications. The 'match between runs' feature in MaxQuant was used to transfer identification to other LC-MS/MS runs based on mass and retention time with a maximum deviation of 0.7 min. Quantifications were performed using a label-free algorithm as previously described.[89] Data analysis was performed using Perseus software (version 1.6.1.3). Eluate co-AP proteins identified with a mean Log_2 ratio ($protein_{His}$/WT) >3-fold change and having a Andromeda confidence score >100[54] in three independent biological replicates were analyzed, while gel-slice proteins identified with a mean Log_2 transformed LFQ score >23 and present in four biological replicates were analyzed.

QUANTIFICATION AND STATISTICAL ANALYSIS

Statistical significance was determined by unpaired t-test using the GraphPad Prism 7, except for the bacterial growth parameters, which was done by Anova and Dunnett post-tests in the aforementioned opm R package. Statistical significance is reported in the figures and legends.

Current Biology, Volume *33*

Supplemental Information

Intracytoplasmic-membrane development in alphaproteobacteria involves the homolog of the mitochondrial crista-developing protein Mic60

Sergio A. Muñoz-Gómez, Lawrence Rudy Cadena, Alastair T. Gardiner, Michelle M. Leger, Shaghayegh Sheikh, Louise B. Connell, Tomáš Bilý, Karel Kopejtka, J. Thomas Beatty, Michal Koblížek, Andrew J. Roger, Claudio H. Slamovits, Julius Lukeš, and Hassan Hashimi

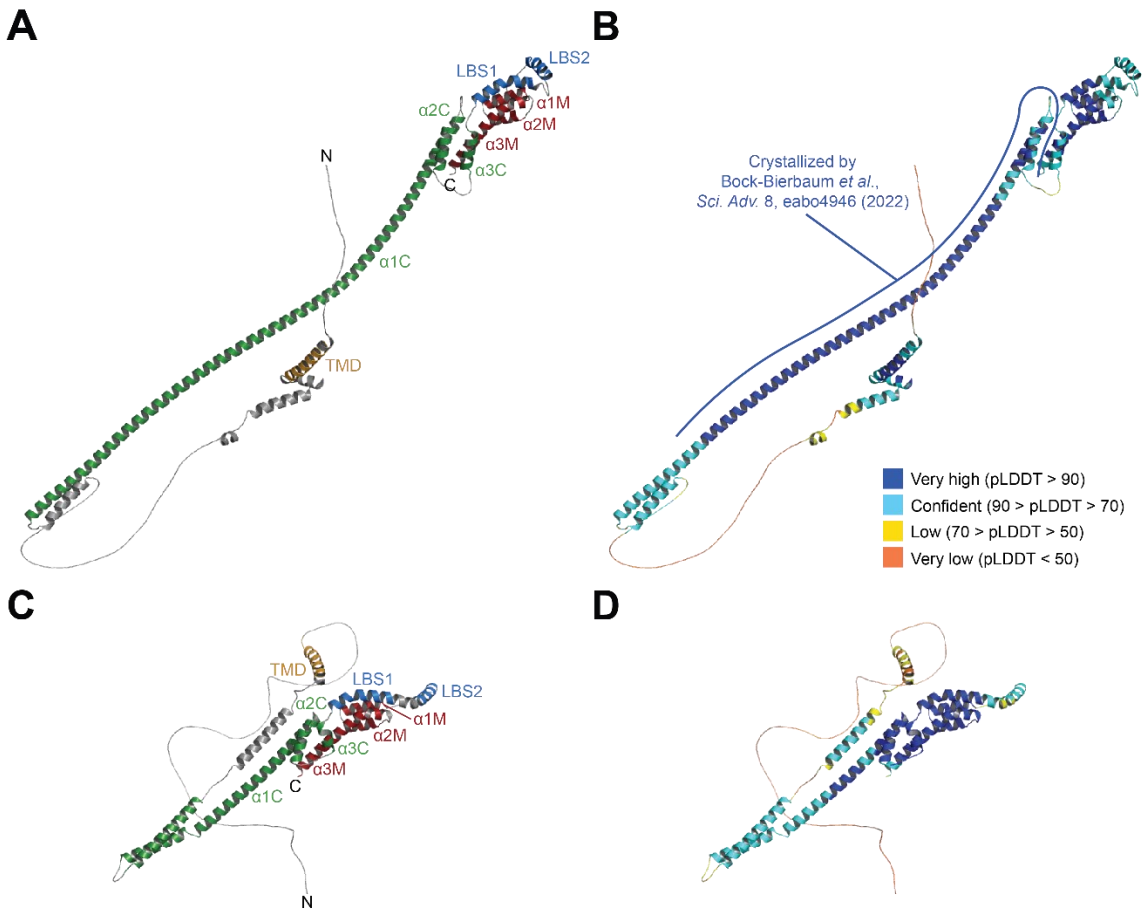

Figure S1. AlphaFold2 predictions of mitochondrial and alphaproteobacterial Mic60 homologs. Related to Figure 2. (**A**) Predicted tertiary structure of the Mic60 homolog of the yeast *L. thermotolerans*. α-helices are colored according to domain (mitofilin in red, LBS1 and LBS2 in blue, middle coiled coils in green, and transmembrane segment in orange) and follow the coordinates predicted by JPred4. (**B**) Predicted tertiary structure of the Mic60 homolog of the yeast *L. thermotolerans* colored by the pLDDT scores, which denote confidence of predicted structure. The long α1C helix (207-382) whose structure was experimentally resolved by Bock-Bierbaum *et al*. (2022) is indicated. (**C**) Predicted tertiary structures of the Mic60 homolog of the alphaproteobacterium *R. sphaeroides*. (**D**) Predicted tertiary structure of the Mic60 homolog of the alphaproteobacterium *R. sphaeroides* colored by the pLDDT scores.

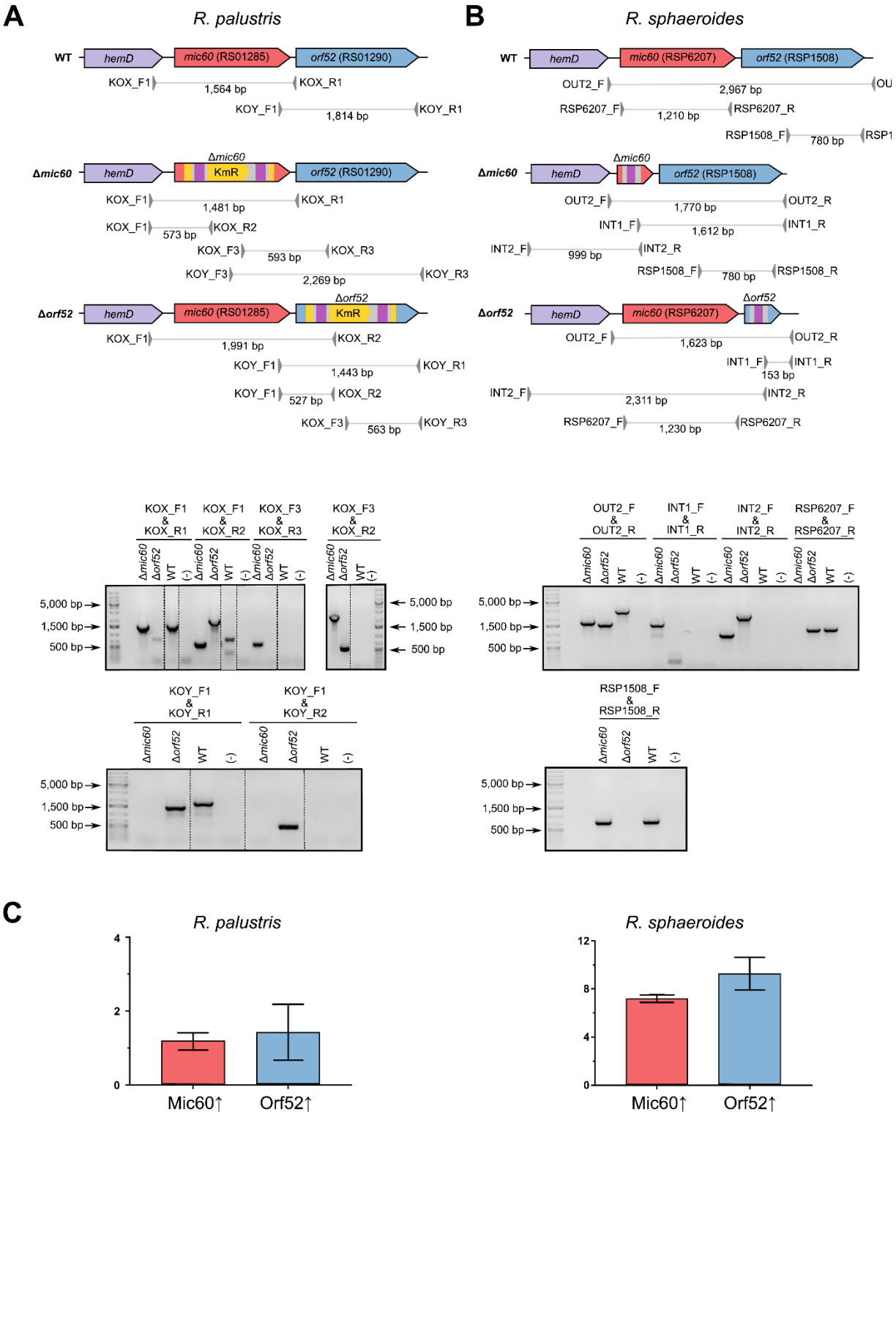
A
R. palustris
WT
hemD
mic60 (RS01285)
orf52 (RS01290)
KOX_F1
1,564 bp
KOX_R1
KOY_F1
1,814 bp
KOY_R1
Δmic60
hemD
Δmic60
KmR
orf52 (RS01290)
KOX_F1
1,481 bp
KOX_R1
KOX_F1
573 bp
KOX_R2
KOX_F3
593 bp
KOX_R3
KOY_F3
2,269 bp
KOY_R3
Δorf52
hemD
mic60 (RS01285)
Δorf52
KmR
KOX_F1
1,991 bp
KOX_R2
KOY_F1
1,443 bp
KOY_R1
KOY_F1
527 bp
KOX_R2
KOX_F3
563 bp
KOY_R3
B
R. sphaeroides
WT
hemD
mic60 (RSP6207)
orf52 (RSP1508)
OUT2_F
2,967 bp
RSP6207_F
1,210 bp
RSP6207_R
RSP1508_F
780 bp
Δmic60
hemD
Δmic60
orf52 (RSP1508)
OUT2_F
1,770 bp
OUT2_R
INT1_F
1,612 bp
INT1_R
INT2_F
999 bp
INT2_R
RSP1508_F
780 bp
RSP1508_R
Δorf52
hemD
mic60 (RSP6207)
Δorf52
OUT2_F
1,623 bp
OUT2_R
INT1_F
153 bp
INT1_R
INT2_F
2,311 bp
INT2_R
RSP6207_F
1,230 bp
RSP6207_R
KOX_F1 & KOX_R1
KOX_F1 & KOX_R2
KOX_F3 & KOX_R3
KOX_F3 & KOX_R2
Δmic60
Δorf52
WT
(-)
5,000 bp
1,500 bp
500 bp
OUT2_F & OUT2_R
INT1_F & INT1_R
INT2_F & INT2_R
RSP6207_F & RSP6207_R
KOY_F1 & KOY_R1
KOY_F1 & KOY_R2
RSP1508_F & RSP1508_R
C
R. palustris
4
2
0
Mic60↑
Orf52↑
R. sphaeroides
12
8
4
0
Mic60↑
Orf52↑

Figure S2. Verification of *mic60* and *orf52* knockout strains and IPTG-induced overexpression of Mic60 and Orf52. Related to Figure 3. A-B. PCR assays confirm the disruption of the *mic60* and *orf52* genes in *R. palustris* (**A**) and *R. sphaeroides* (**B**). Genomic contexts of the relevant loci for the WT, Δ*mic60* and Δ*orf52* strains shown on top, with primer pairs and their expected amplicon sizes shown below each schematic gene arrangement. Lower panel shows each PCR amplicon from each strain (labelled above gel) after agarose gel electrophoresis. Size markers shown either to the left or right of the gel. (**C**) Real time PCR showing relative abundancies of Mic60 and Orf52 mRNAs in *R. palustris* (left) and *R. sphaeroides* (right) strains grown in the presence of the expression induction agent IPTG relative to the same strains grown without IPTG. Error bars show standard deviation from three replicates of assayed induced and non-induced cells.

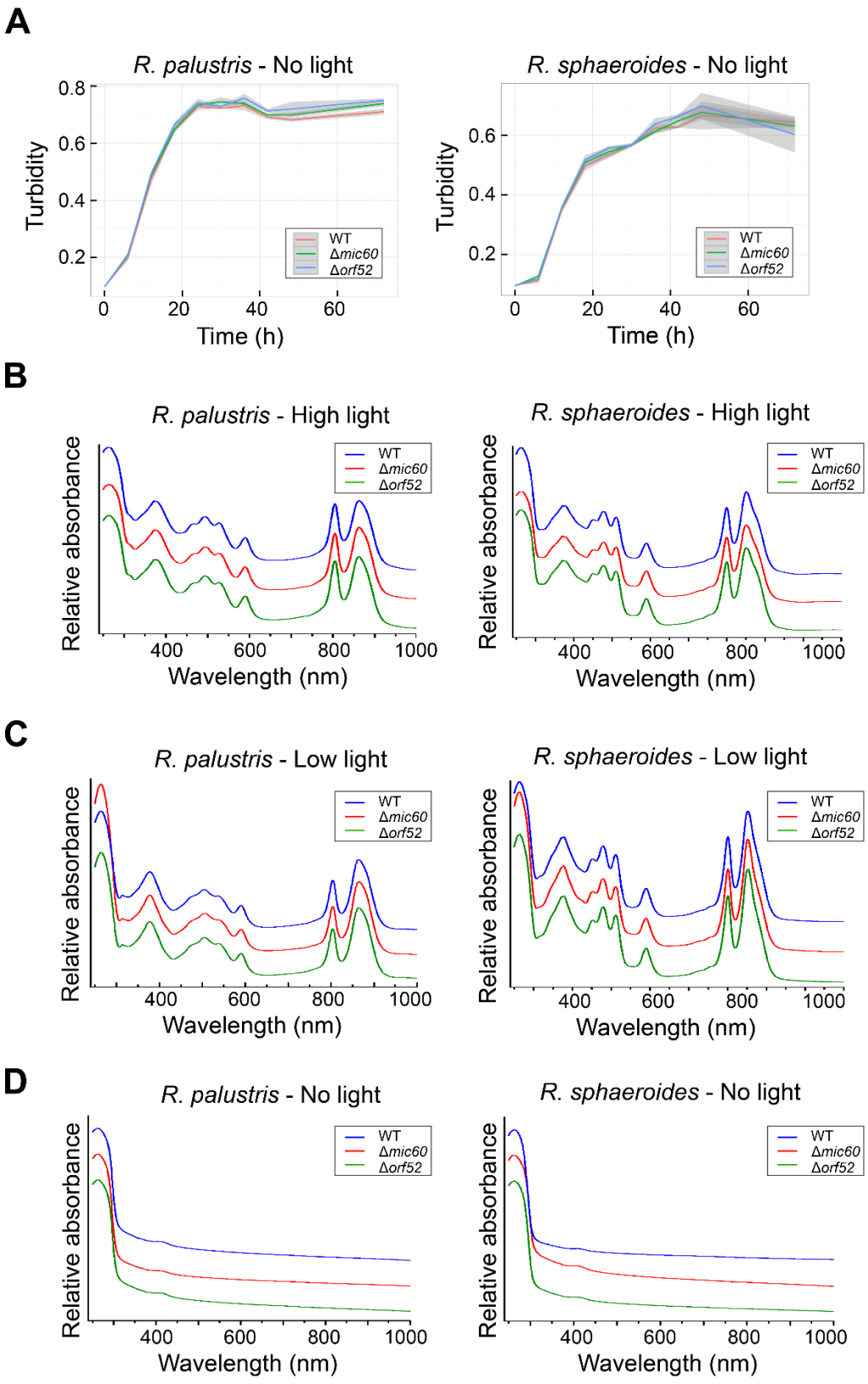
A
R. palustris - No light
R. sphaeroides - No light
Turbidity
Time (h)
WT
Δmic60
Δorf52
B
R. palustris - High light
R. sphaeroides - High light
Relative absorbance
Wavelength (nm)
C
R. palustris - Low light
R. sphaeroides - Low light
D
R. palustris - No light
R. sphaeroides - No light

Figure S3. Chemoheterotrophic growth and absorption spectra of *mic60* and *orf52* knockout strains. Related to Figure 3. (**A**) Growth curves of *R. palustris* (left) and *R. sphaeroides* (right) under chemoheterotrophic conditions in the presence of malate to feed the respiratory chain. Figure labelled as in Figs. 3A-D. Absorption spectra of whole *R. palustris* (left) and *R. sphaeroides* (right) WT and knockout strains grown photoheterotrophically at either high light (**B**) or low light (**C**), as well as chemoheterotrophically in the dark and presence of oxygen (**D**).

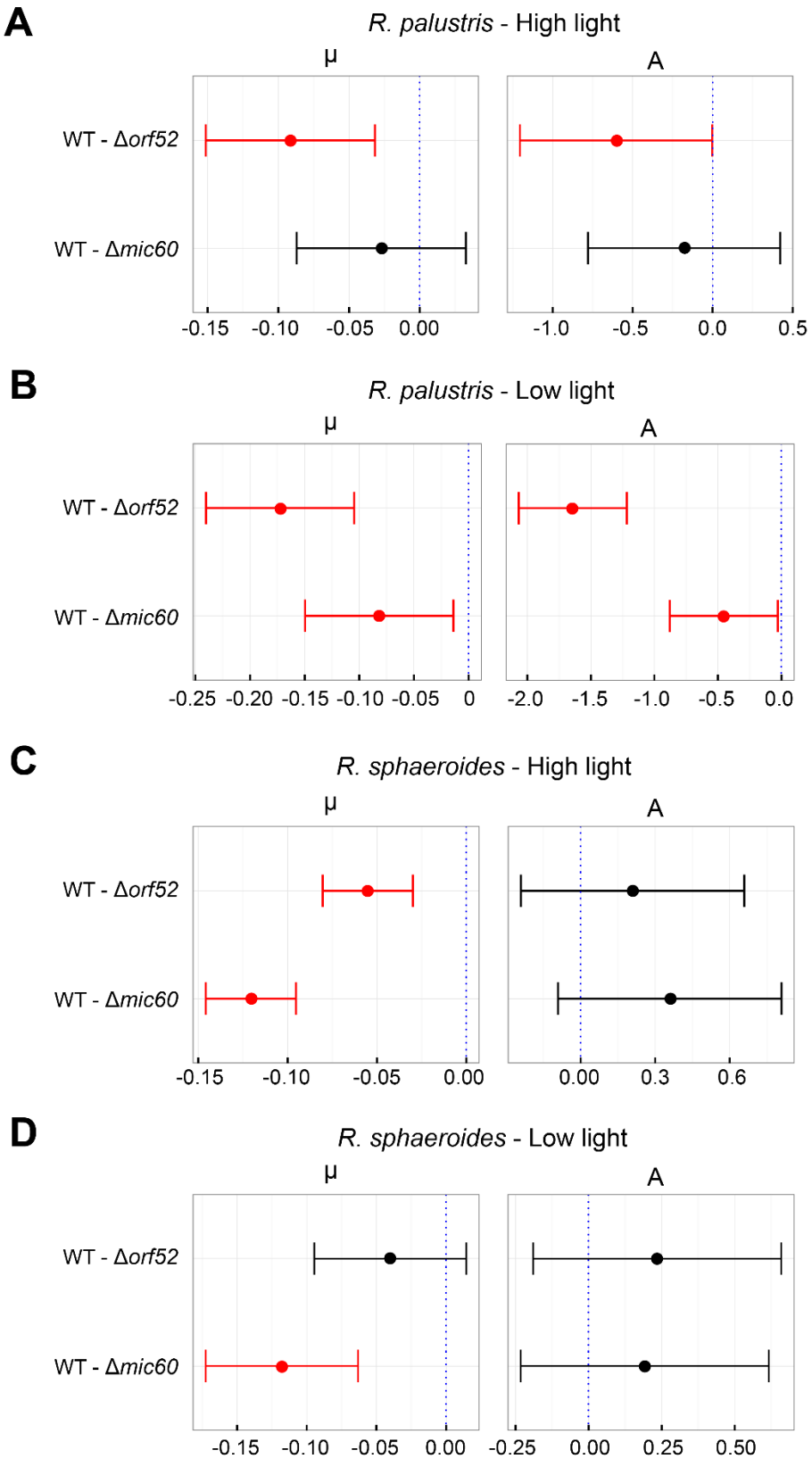
A
R. palustris - High light
μ
A
WT - Δorf52
WT - Δmic60
-0.15 -0.10 -0.05 0.00
-1.0 -0.5 0.0 0.5
B
R. palustris - Low light
μ
A
WT - Δorf52
WT - Δmic60
-0.25 -0.20 -0.15 -0.10 -0.05 0
-2.0 -1.5 -1.0 -0.5 0.0
C
R. sphaeroides - High light
μ
A
WT - Δorf52
WT - Δmic60
-0.15 -0.10 -0.05 0.00
0.00 0.3 0.6
D
R. sphaeroides - Low light
μ
A
WT - Δorf52
WT - Δmic60
-0.15 -0.10 -0.05 0.00
-0.25 0.00 0.25 0.50

Figure S4. 95% family-wise confidence intervals for pairwise comparisons of wild type and knockout strains. Related to Figure 3. Pairwise comparisons of estimated growth rate (μ) and abundance (A) between wild type and Δ*mic60* and wild type and Δ*orf52* for *R. palustris* in low (**A**) and high light (**B**) and for *R. spaheroides* in low (**C**) and high light (**D**). Estimated differences on the x-axis. Red color indicates a statistical significant difference for the pairwise comparisons. Blue dashed line marks no estimated difference in the inferred parameter.

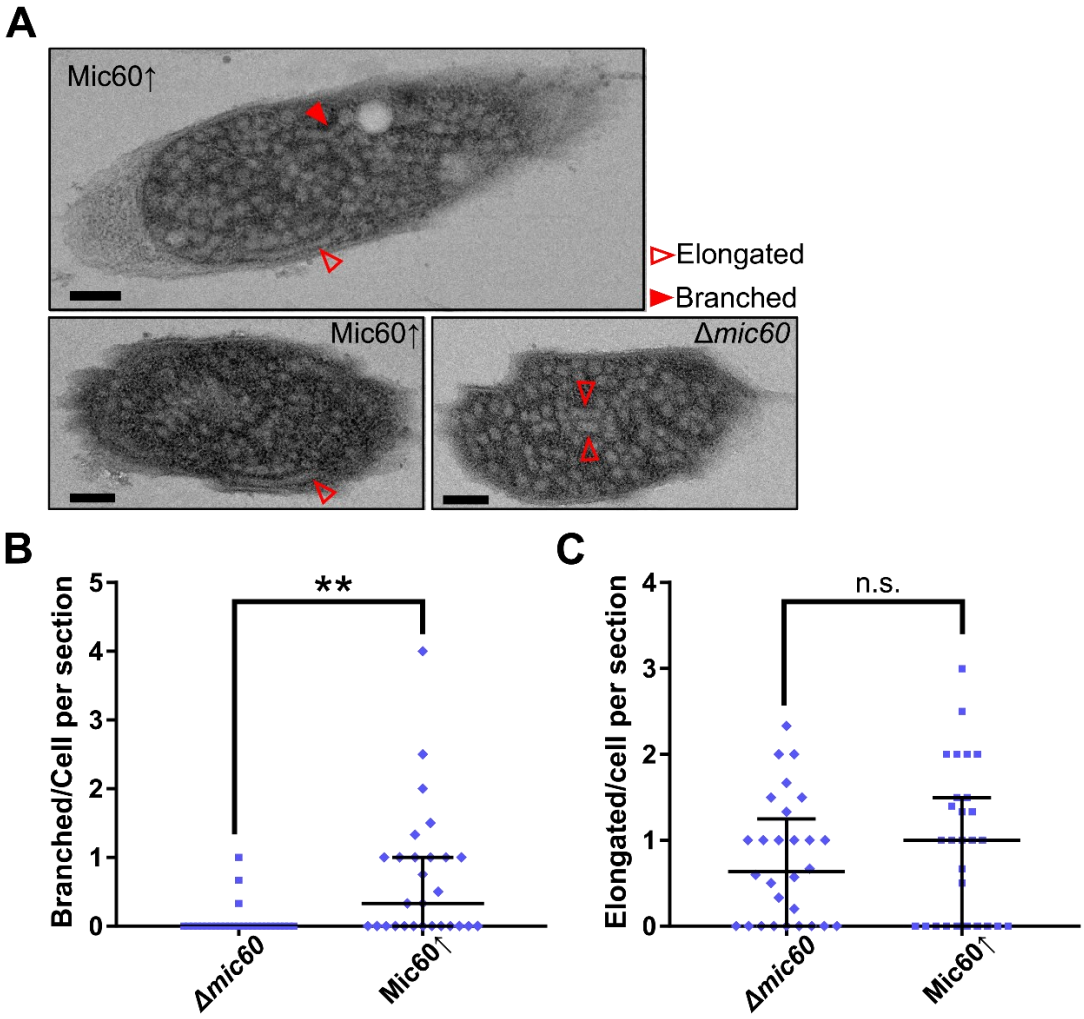

Figure S5. Quantification of branched ICM occurrence in *R. sphaeroides mic60* knockout (Δ*mic60*) and Mic60 overexpression (Mic60↑) strains. Related to Figure 3. (**A**) Representative transmission electron micrographs of elongated (hollow arrowhead) and branched (solid arrowhead) ICMs. Imaged strain indicated in upper corner of micrographs. Scale bar, 100 nm. Scatter plots showing blind quantification of branched (**B**) and elongated (**C**) ICMs. Middle bar shows median value and whiskers denote interquartile range. Statistical significance: **, P<0.01; n.s., not significant.

A

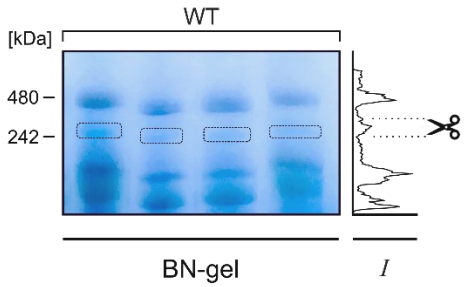

B

Mic60

Protein	Fold change	UPB	ICM	Membrane integral	250 kDa complex	Mol. weight [kDa]
Mic60	245.13	○	○*	●	●	43.8
PAS sensor Signal Tranduction Histidine Kinase	9.57	○	○	○	○	105.0
BamA	9.09	●	●	●	●	88.2

C

Orf52

Protein	Fold change	UPB	ICM	Membrane integral	250 kDa complex	Mol. weight [kDa]
Transcriptional regulator, LuxR family	46.21	○	○	○	○	26.9
RSP_7517	35.62	○	○	●	◍	4.8
Ribonucleoside-diphophate reductase class II	31.75	○	○	○	○	132.0
3-oxoacyl-(acyl-carrier-protein) reductase	26.75	○	○	○	○	25.0
RSP_3919 (plasmid)	23.63	○	○	○	○	37.5
BamA	22.38	●	●	●	●	88.2
Transcriptional regulator, MarR family	22.15	○	○	○	○	19.0
OM Efflux protein	18.52	●	●	●	●	49.7
PAS sensor Signal Tranduction Histidine Kinase	12.49	○	○	○	○	104.9
Transcriptional regulator, winged helix family	9.50	○	○	○	○	26.1
Orf52	8.50	●	●	●	●	52.5
Translation enlongation factor 2	8.42	●	○	○	◍	77.7
Peptidyl-tRNA hydrolase	8.32	○	○	○	○	24.2

D

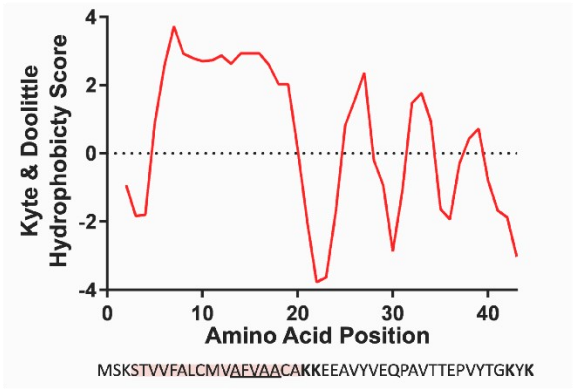

Figure S6. Proteomic analysis of isolated ICMs plus Mic60 and Orf52 interactomes. Related to Figure 5. (**A**) Blue native gel resolved detergent-solubilized ICMs from *R. sphaeroides* WT in which the ~250 kDa band (boxed) was excised in quadruplet for subsequent MS analysis. To right of gel is a histogram of the Coomassie-stained band intensities (*I*) along the vertical axis of the run. The scissors denote the ~250 kDa band intensity signal. (**B-C**)**.** A list of all proteins, including excluded contaminants, found within the enriched protein area of the volcano plots in in Figure 4A-B for Mic60 (**B**) and Orf52 (**C**). Columns as described in legend of Figure 5C-D. Note the presence of likely contaminant found in both APs, PAS-fold containing histidine kinase (PAS), which is a large protein amenable to LC-MS/MS in contrast to RSP_7517 and not found in any of our requisite proteomes. (**D**) Kyle and Doolittle hydropathy plot of RSP_7517, whose amino acid sequence is given below. Predicted transmembrane domain shaded and a potential oligomerization motif AxxxA underlined. Lysine (K) residues recognized by trypsin protease are in bold.